

Numerical modeling of self-channeling granular flows and of their levee-channel deposits

A. Mangeney,^{1,2} F. Bouchut,³ N. Thomas,⁴ J. P. Vilotte,¹ and M. O. Bristeau⁵

Received 26 January 2006; revised 13 October 2006; accepted 18 December 2006; published 17 May 2007.

[1] When not laterally confined in valleys, pyroclastic flows create their own channel along the slope by selecting a given flowing width. Furthermore, the lobe-shaped deposits display a very specific morphology with high parallel lateral levees. A numerical model based on Saint Venant equations and the empirical variable friction coefficient proposed by Pouliquen and Forterre (2002) is used to simulate unconfined granular flow over an inclined plane with a constant supply. Numerical simulations successfully reproduce the self-channeling of the granular lobe and the levee-channel morphology in the deposits without having to take into account mixture concepts or polydispersity. Numerical simulations suggest that the quasi-static shoulders bordering the flow are created behind the front of the granular material by the rotation of the velocity field due to the balance between gravity, the two-dimensional pressure gradient, and friction. For a simplified hydrostatic model, competition between the decreasing friction coefficient and increasing surface gradient as the thickness decreases seems to play a key role in the dynamics of unconfined flows. The description of the other disregarded components of the stress tensor would be expected to change the balance of forces. The front's shape appears to be constant during propagation. The width of the flowing channel and the velocity of the material within it are almost steady and uniform. Numerical results suggest that measurement of the width and thickness of the central channel morphology in deposits in the field provides an estimate of the velocity and thickness during emplacement.

Citation: Mangeney, A., F. Bouchut, N. Thomas, J. P. Vilotte, and M. O. Bristeau (2007), Numerical modeling of self-channeling granular flows and of their levee-channel deposits, *J. Geophys. Res.*, 112, F02017, doi:10.1029/2006JF000469.

1. Introduction

[2] When not laterally confined in valleys, pyroclastic flows propagate with a tongue shape and subparallel borders, creating their own channel along a slope by selecting a given flowing width that is strongly dependent on the underlying topography. Furthermore, the lobe-shaped deposits exhibit a very specific morphology with parallel lateral levees (about 1 m high) enriched in large blocks while the central channel is lower and composed mainly of smaller particles [e.g., *Nairn and Self*, 1978; *Calder et al.*, 2000; *Saucedo et al.*, 2002; *Ui et al.*, 1999; *Rodriguez-Elizarraras et al.*, 1991; *Wilson and Head*, 1981]. Such channeled flows leaving a levee-channel morphology in deposits on the slope are also observed in very different

environments and for flows involving completely different materials such as landslide deposits on Mars [*Mangold et al.*, 2003; *Treiman and Louge*, 2004] or submarine landslides [*Klaucke et al.*, 2004]. Although lava flows have a totally different mechanical behavior, similar morphological features are observed in their deposits [*Sakimoto and Gregg*, 2001; *Quarenì et al.*, 2004].

[3] Several explanations have been proposed for the channeling of these unconfined flows and their levee-channel morphology: Bingham rheology leading to lateral static zones as is the case for lava flows [*Yamamoto et al.*, 1993; *Quarenì et al.*, 2004; *Mangold et al.*, 2003], drainage of the central part of the deposit with static levees [*Rowley et al.*, 1981] and differential deflation and differential fluidization of borders during emplacement due to polydispersity of the particles [*Rowley et al.*, 1981; *Wilson and Head*, 1981]. The levee-channel morphology observed on Martian landslides was first interpreted as indicating the presence of water during emplacement [*Malin and Edgett*, 2000]. Similarly, assuming a Bingham rheology, *Mangold et al.* [2003] deduced from the analysis of levees that the observed gullies over large Martian dunes involve flows with a significant proportion of fluids. On the other hand, *Treiman and Louge* [2004] refer to dry flows to explain the levee-channel morphology of Martian gullies. Field measurements have been performed on such deposits, but the question remains as to what extent these measurements

¹UMR 7580, Institut de Physique du Globe de Paris, Université Denis Diderot, CNRS, Paris, France.

²Now at Institute for Nonlinear Science, University of California, San Diego, La Jolla, USA.

³Département de Mathématiques et Applications, Ecole Normale Supérieure, CNRS, Paris, France.

⁴Institut Universitaire des Systèmes Thermiques Industriels, CNRS, Marseille, France.

⁵Institut National de Recherche en Informatique et en Automatique, Rocquencourt, France.

provide information on the mechanical properties and dynamics of the flow during emplacement. Which geomorphologic features (such as width or thickness of the central channel or levees) are almost independent with respect to time and the distance from the supply and therefore pertinent to characterize the flow?

[4] Laboratory experiments show that the channeling of unconfined flows and the formation of a levee-channel morphology in deposits may be explained by referring to dry granular flows alone [e.g., McDonald and Anderson, 1996; Félix and Thomas, 2004]. The channeling and the formation of levees are strongly related to the free lateral boundaries and to the highly unsteady stopping stage. However, while the steady laterally uniform flow regime of confined granular materials along inclined planes has been largely characterized [Gray et al., 1999; Pouliquen, 1999], the behavior of granular materials under unsteady and nonuniform conditions is still an open question. The experiments of Félix and Thomas [2004] on unconfined dry granular flows over an inclined plane show that the formation of levees results from the combination of lateral static zones on each border of the flow (shoulders) and the drainage of the central part of the flow after the supply stops. Particle segregation features are also created during the flow, corresponding to those observed in the deposits of pyroclastic flows. When the range of sizes of the polydisperse material is reduced, the morphology is smoothed but never reaches a flat surface [Félix and Thomas, 2004]. However, a perfectly monodispersed material could not be used in experimental work, and it is therefore possible that polydispersity is a necessary condition for the formation of the levee-channel morphology. Moreover, it is uncertain whether this morphology can be obtained without assuming Bingham rheology, for example using a Coulomb friction law, better suited to describing the flow of dry granular matter [see, e.g., Hutter et al., 1995]. It is also unknown how the shoulders channeling the flow are created and if the associated spatial nonuniformity is linked to the hysteretic character of the granular material, i.e., its capacity to be either in a static or flowing state depending on the history of the dynamics.

[5] The aim of this paper is to shed light on these questions by assessing whether a simple depth-averaged model based on Saint Venant equations and Coulomb type friction is able to reproduce the complex behavior of unconfined granular flows with channel formation and levee-channel morphology in deposits. A simple hydrostatic model involving the empirical variable friction coefficient proposed by Pouliquen and Forterre [2002] is used here. As the other friction laws proposed in the literature for dry granular flows, Pouliquen and Forterre's empirical flow rule is obviously oversimplified to reproduce the natural complexity where polydisperse, multiphase materials are involved. The following simulations strongly depend on the peculiar features of this empirical friction law. The case treated in this paper, namely dry granular flows without polydispersity effects over inclined plane, is very simple and therefore quite different from typical geophysical cases such as pyroclastic flows and debris flows involving effects like grain size segregation and variable liquefaction or fluidization [e.g., Iverson and Vallance, 2001]. The question

addressed here is whether self-channeling flows and levee-channel morphology can be obtained for this simple case.

[6] Simple continuum hydrodynamic models, based on the long-wave approximation (hereafter called LWA) [Savage and Hutter, 1989] and Saint Venant equations, have been shown to reproduce the basic features of both experimental dense granular flows along inclined planes and geological flows over real topographies [e.g., Denlinger and Iverson, 2001; Naaïm et al., 1997; Pastor et al., 2002; McDougall and Hungr, 2004; Pouliquen and Forterre, 2002; Mangeney-Castelnau et al., 2003; Pitman et al., 2003; Denlinger and Iverson, 2004; Iverson et al., 2004; Sheridan et al., 2007; Lucas and Mangeney, 2007]. Continuum models are expressed in terms of the change of the vertically averaged velocity field and of the associated vertical length scale h , i.e., the avalanche thickness, and describe hydrostatic imbalance [Mangeney-Castelnau et al., 2003] or nonhydrostatic plasticity and friction effects [Savage and Hutter, 1989]. The models assume an averaged friction dissipation described phenomenologically by Coulomb's friction law with a constant [e.g., Hutter et al., 1995; Naaïm et al., 1997] or velocity- and thickness-dependent [Pouliquen, 1999; Douady et al., 1999] friction coefficient. More sophisticated models have been recently proposed by Denlinger and Iverson [2004] based on Mohr-Coulomb plasticity theory. Although the friction law describing the behavior of steady flows has been relatively well refined by laboratory experiments, the behavior of a granular mass at small Froude numbers (i.e., at low velocities) is still an open question. Hysteresis is an important characteristic of granular slope stability. Indeed, a granular slope starts to flow when its inclination reaches a typical avalanche angle θ_a and comes to rest once its slope reaches another so-called repose angle $\theta_r < \theta_a$. The hysteretic behavior occurs for inclination angles $\theta \in [\theta_r, \theta_a]$ [e.g., Pouliquen and Forterre, 2002; Daerr and Douady, 1999]. The metastability of a granular slope in this range of angles has been shown to be very complex and requires a biphasic description of strong and weak contact networks in the granular pile [Deboeuf et al., 2005a, 2005b]. In the macroscopic depth-averaged formulation inherent to the long-wave approximation, the empiric description of this metastability remains uncertain. Still, the formation of channeling flows with the construction of nearly static shoulders as well as the existence of levees are likely to be strongly related to the behavior of granular materials near the stopping or destabilization phases. Because unconfined flows continuously juggle between static and flowing conditions, their numerical simulation can be used to improve the macroscopic description of the metastable behavior of granular flows which is still an open question.

[7] We first briefly describe, in section 2, the experimental results that motivated this study. After a description of the model and the flow law in section 3, a simulation of experimental results of confined granular flow over an inclined plane with constant supply and its deposit after stopping the supply is described in section 4 in order to check the model in a configuration much simpler than the case of free-boundary flows. A numerical simulation of the channeling process and the formation of levees is performed in section 5, providing new insight into the experimental observations based on a qualitative comparison between

experimental and numerical results. In section 6, the dynamics of the channeling flows and the forces involved are investigated to shed light on the mechanism generating the complex behavior of unconfined flows.

2. Experimental Evidence

[8] *Félix and Thomas* [2004] have shown that unconfined flows of dry granular material over a rough inclined plane with a constant supply reach a steady state, after which the front propagates at a constant velocity, the thickness is quasi-uniform and constant with time and the width of the flow is uniform. The structure of unconfined flow has been shown to be separated into a flowing central channel and two static shoulders on each border of the channel. As the supply stops, the thickness of the channel decreases while the thickness of the static shoulders remains unchanged, leading to a deposit with a levee-channel morphology. Glass beads of diameter 300–400 μm have been used in the experiments with initial flux varying from 6 g s^{-1} to 34 g s^{-1} over an inclined plane 2 m long and 80 cm wide, with slope angles in the range $[25^\circ, 29^\circ]$. Taking a closer look at the dynamics of unconfined flow, recent experiments have shown that granular flow slowly enlarges while its thickness decreases if the supply is maintained for a long duration [*Deboeuf et al.*, 2006].

[9] Although these studies mention the effect of polydispersity, it has not been determined whether segregation is a necessary condition to obtain levees and static shoulders. Moreover, these studies do not provide the precise velocity field within the flow and do not explain the formation of static shoulders at the rear of the front. It seems that the dynamics at the front determine the width but this mechanism has not been investigated. Consequently, no condition can be deduced for the determination of the width, thickness and velocity of the flow for a given flux. In the following, we simulate this type of experiment numerically using a long-wave approximation model. We investigate to what extent such a model is able to shed light on these questions.

3. Model

3.1. Mass and Momentum Conservation

[10] Depth-averaged continuum models have been shown to be useful in reproducing the basic behavior of the flow on sloping topography under experimental or natural conditions [e.g., *Denlinger and Iverson*, 2001; *Naaïm et al.*, 1997; *Pouliquen and Forterre*, 2002; *Mangeney-Castelnau et al.*, 2003, 2005; *Pitman et al.*, 2003]. These models are based on the long-wave approximation, which is appropriate for granular flows over inclined topography given that the characteristic length in the flow direction is much larger than the vertical length, i.e., the avalanche thickness, thereby satisfying the hydrostatic assumption.

[11] A new model has recently been derived by *Bouchut and Westdickenberg* [2004] for gravity driven shallow water flow over an arbitrary two-dimensional (2-D) topography. The model is written in an arbitrary coordinate system for shallow flow over a topography with small curvature. Dimensional analysis has been performed by *Bouchut and Westdickenberg* [2004] in a manner similar to that of *Hutter and coworkers*. The overall idea is to develop the equations

in a fixed reference frame (x, y, z) , for example horizontal/vertical, as opposed to the equations developed by *Hutter and coworkers* in a variable reference frame linked to the topography. However, the shallowness assumptions are still imposed in the local reference frame (X, Y, Z) linked to the topography (Figure 1). Indeed, to satisfy the hydrostatic assumption for shallow flow over inclined topography, it is the acceleration normal to the topography that must be neglected compared to the gradient of the pressure normal to the topography. The reference frame is shown in Figure 1. The 2-D horizontal coordinate vector is $\mathbf{x} = (x, y) \in \mathbb{R}^2$ and the topography is described by the scalar function $b(x, y)$ with a 3-D unit upward normal vector

$$\vec{n} = \left(-\frac{\nabla_{\mathbf{x}} b}{\sqrt{1 + \|\nabla_{\mathbf{x}} b\|^2}}, \frac{1}{\sqrt{1 + \|\nabla_{\mathbf{x}} b\|^2}} \right) \equiv (-\mathbf{s}, c) \in \mathbb{R}^2 \times \mathbb{R}. \quad (1)$$

The scalar $c = \cos \theta$ is indeed the cosine of the angle between the vertical direction and the normal \vec{n} . In our notation, the 3-D vectors are denoted by $\vec{\cdot}$, whereas the 2-D vectors in the inclined plane tangent to the topography are written in bold. The equations take into account all the components of the curvature tensor contrary to the majority of former studies which refer only to the curvature radius R_i , $i = x, y$ in the directions in which the equations are written [see, e.g., *Naaïm et al.*, 1997; *Gray et al.*, 1999; *Mangeney-Castelnau et al.*, 2003; *Pitman et al.*, 2003]. The equations are written in their fully general form in Appendix A. For flow over an inclined plane of slope $db/dx = \tan \theta$, the subject of this paper, the curvature tensor can be reduced to the null tensor. In the horizontal/vertical Cartesian coordinate formulation the equations reduce to

$$\frac{\partial h}{\partial t} + c \frac{\partial}{\partial x} (hu) + \frac{\partial}{\partial y} (hv) = 0 \quad (2)$$

$$\frac{\partial u}{\partial t} + cu \frac{\partial u}{\partial x} + v \frac{\partial u}{\partial y} + c \frac{\partial}{\partial x} (ghc) = -g \sin \theta + \tilde{f}_{fx} \quad (3)$$

$$\frac{\partial v}{\partial t} + cu \frac{\partial v}{\partial x} + v \frac{\partial v}{\partial y} + \frac{\partial}{\partial y} (ghc) = \tilde{f}_{fy}, \quad (4)$$

where h is the thickness of the material layer in the direction normal to the topography. The velocity is defined by $\mathbf{u} = (u, v)$, where u and v are respectively the velocity in the direction X of the steepest slope and the horizontal velocity in the transverse direction Y . These equations model the hydrostatic imbalance in presence of a friction force $\tilde{\mathbf{f}}_f = (\tilde{f}_{fx}, \tilde{f}_{fy})$, parallel to the inclined plane. Although equations (3) and (4) are written using terms having the dimensions of acceleration, we will refer to them in the following as forces. Note that introducing the coordinate X in the inclined direction instead of x , i.e., $X = x/c$, gives $c \partial / \partial x = \partial / \partial X$, and (2)–(4) can then be reduced to the classical shallow water equations.

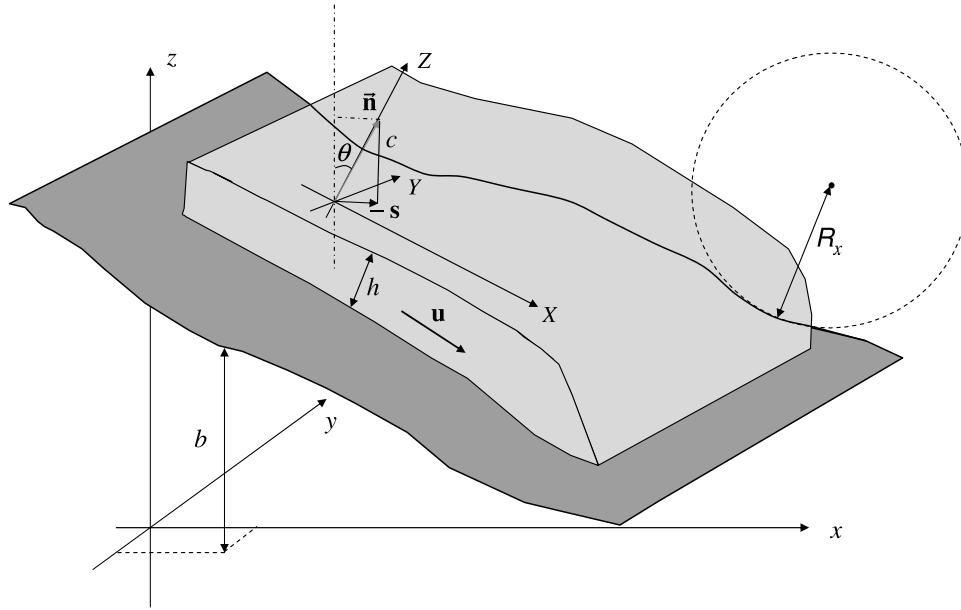


Figure 1. Reference frame and variables used in the model.

[12] The friction force $\tilde{\mathbf{f}}_f$ is equal to the depth-averaged value of the Z derivative of the shear stress, i.e., in one dimension,

$$\tilde{f}_{fx} = \frac{1}{h} \int_0^h \frac{\partial \tau_{xz}}{\partial Z} dZ = \frac{1}{h} (\tau_{xz}|_{Z=h} - \tau_{xz}|_{Z=0}). \quad (5)$$

Here τ_{xz} corresponds to the real shear stress divided by ρ , the mass density, and will be called hereafter shear stress for sake of simplicity. The free surface condition imposes that the component of the stress in the direction tangent to the free surface is equal to zero at $Z = h$. The term $\tau_{xz}|_{Z=0}$, combined with terms obtained when depth averaging the other components of the stress tensor thus disappears from the depth-averaged equations [see, e.g., Mangeney-Castelnau *et al.*, 2003]. As a result, the value of depth-averaged Z derivative of the shear stress is replaced by the opposite of the value of the basal shear stress $-\tau_{xz}|_{Z=0}$. Once the equations have been depth averaged, the interpretation of the friction force \mathbf{f}_f as the friction occurring at the base of the flow is therefore not obvious, and requires at least implicit assumptions on the Z profile of the shear stress.

3.2. Flow Law

[13] The appropriate flow law to describe dissipation in dry granular flows is still under debate. Among the various attempts to tackle this problem, it is possible to distinguish two approaches, at least when considering those used in avalanche modeling. In the pioneer approach proposed by Savage and Hutter [1989] (hereinafter referred to as SH), the components of the stress tensor are deduced from the Coulomb plasticity criterium. The resulting flow law takes into account the anisotropy of normal stresses by the introduction of a factor k depending phenomenologically on both a constant basal friction angle δ and a constant internal friction angle ϕ that are to be independently determined experimentally. The importance of the factor k is still an open question. In rapid granular flows in which

the surface gradients are small, the nonhydrostatic effects (i.e., anisotropy of normal stresses) seem to be negligible [Ertas *et al.*, 2001]. However, under quasi-static conditions or near the margin of developing or already-emplaced deposits, where surface gradients can be large, these effects are expected to be significant [Iverson *et al.*, 2004]. Today, an accurate derivation of the 3-D equations based on the SH theory over an arbitrary topography is still lacking [see, e.g., Pirulli *et al.*, 2007]. Furthermore, the stresses on planes normal to the bed are commonly neglected in models of granular flows. A more sophisticated model, motivated by the Rankine equations, has been recently developed by Denlinger and Iverson [2004], that involves numerical calculation of the entire stress tensor for depth-averaged flow. Simulations of experimental results of granular flows over a complex topography highlight the importance of the stresses normal to the bed [Iverson *et al.*, 2004].

[14] The second approach uses a purely phenomenological representation of the dissipation in granular flows. A parameterization of the so-called “basal” friction coefficient $\mu = \tan \delta$ as a function of the avalanche mean velocity and the thickness is obtained from experiments on steady uniform flows over inclined planes [Douady *et al.*, 1999; Pouliquen, 1999]. This μ parameterization has been introduced in depth-averaged long-wave equations together with strong assumptions on the components of the stress tensor: isotropy of normal stresses and negligible stresses on planes normal to the bed [Pouliquen and Forterre, 2002; Mangeney-Castelnau *et al.*, 2003]. In the context of granular media, this is an exceedingly bold assumption, as experimental data and Coulomb theory show that bed-parallel stresses in quasi-static granular media are not simply due to hydrostatic pressure [e.g., see Sokolovski, 1965]. Despite all these limitations, the resulting model is able to describe the experimental observation of steady uniform flows over a plane for a given range of inclination angles contrary to the SH-type models involving a constant friction angle δ . Indeed, the equation of a steady uniform flow deduced from

equation (3) combined with the Coulomb friction law (7) described in the following reads

$$\mu = \tan \theta, \quad (6)$$

indicating that the friction force exactly balances the force of gravity. This equilibrium is also obtained with SH's equations even if the stresses normal to the bed are introduced in a way similar to that of *Iverson and Denlinger* [2001]. In fact, in the case of steady uniform flow $\partial h / \partial x$ and $\partial h / \partial y$ are equal to zero and the terms related to anisotropy of normal stresses or stresses on planes normal to the bed disappear.

[15] However, the physical basis of this μ parameterization is still an open question. In particular, this parameterization is obtained by assuming that all the dissipation is described by the term $\tilde{\mathbf{f}}_f$ in equations (3) and (4). The question, however, is: does this relation hold only because the other components of the stress tensor or the friction at the lateral walls are neglected or because the dissipation in granular flows is more complicated than the proposed Coulomb-type models? Despite all these uncertainties, we try here, in a first attempt to model the process of levee formation by unconfined granular flows, to reproduce the observed channeling of the flow and the levee-channel morphology by simply using this μ parameterization. The idea is to analyze the balance of the forces that governs the mechanics of self-channeling flows when this phenomenological representation of dissipation effects is introduced in the model. All the limitations due to the strong assumptions related to the disregarded components of the stress tensor have to be kept in mind when analyzing the following results.

[16] Unlike fluids, granular materials can sustain a given stress without deforming. The transition between a static state ($\mathbf{u} = 0$) and a flowing state is generally simply modeled in depth-averaged models by introducing a Coulomb threshold σ_c . The motion is allowed only if the norm of the driving forces $\|\tilde{\mathbf{f}}_f\|$ exceeds the Coulomb threshold [*Mangeney-Castelnau et al.*, 2003]. In the model (3)–(4), $\tilde{\mathbf{f}}_f$ is expressed as

$$\begin{aligned} \|\tilde{\mathbf{f}}_f\| \geq \sigma_c &\Rightarrow \tilde{\mathbf{f}}_f = -gc\mu \frac{\mathbf{u}}{\|\mathbf{u}\|} \\ \|\tilde{\mathbf{f}}_f\| < \sigma_c &\Rightarrow \mathbf{u} = \mathbf{0}, \end{aligned} \quad (7)$$

where $\sigma_c = gc\mu$. When the material exceeds the Coulomb threshold, the Coulomb friction law states that when flowing, the friction force has a direction opposite to the averaged tangential velocity field and the amplitude of the friction force is governed by the total overall pressure and the friction coefficient μ . The friction force $\tilde{\mathbf{f}}_f$ is multivalued for $(u, v) = (0, 0)$ when the flow history is not known. For this reason, the friction has been regularized numerically as described in Appendix B (equations (B12) and (B16)). As a result, for small velocities, the direction of the friction is given by the driving forces related to the h gradient and gravity. It is well known that the failure surface develops within the granular mass at the initiation of the flow and that the arrest phase involves both a horizontal and a vertical propagation of the transition between static and flowing materials. The above classical approach (7) to describe the

initiation or stopping of the flow by simply referring to the “basal” coefficient of friction is difficult to justify when both basal and internal dissipation are taken into account in the model.

[17] Near the transition between the static (jammed) and the flowing (unjammed) state, the behavior of granular material is still an open question. In this so-called metastable regime, the jammed state of the granular material is conditionally stable and an avalanche can be triggered by perturbations of finite amplitude [*Daerr and Douady*, 1999]. The different characteristic angles of stability of granular systems reflect this metastability. In the case studied here, where quasi-static zones develop near the margins of the granular lobe, the behavior in the metastable regime is expected to play a key role in the dynamics. Is it necessary to take into account two different friction angles corresponding to the avalanche and repose angles to simulate self-channeling flows? Is the metastable regime involved during the formation of self-channeling flows?

[18] These questions will be investigated here by using the μ parameterization proposed by [*Pouliquen and Forterre*, 2002] which takes into account the typical hysteresis behavior of granular matter. Let us recall here the main features of this phenomenological approach. Steady uniform flows over rough bedrock have been observed experimentally for a range of inclination angles, making it possible to identify a scaling law relating the thickness and mean velocity of the flow [*Pouliquen*, 1999]. This scaling law or flow rule involves two empirical functions that are expected to contain fundamental information on the friction properties of the material and of its interaction with the rough plane: (1) the function relating the slope angle θ of an inclined plane to the thickness staying on the plane $h_{stop}(\theta)$ and (2) the function relating the slope angle θ to the minimum thickness of an initially at rest granular layer necessary to generate a flow on the same plane $h_{start}(\theta)$.

[19] These empirical functions

$$h_{stop}(\theta) = L \frac{\tan \delta_2 - \tan \theta}{\tan \theta - \tan \delta_1} \quad (8)$$

$$h_{start}(\theta) = L \frac{\tan \delta_4 - \tan \theta}{\tan \theta - \tan \delta_3} \quad (9)$$

involve the parameters δ_i and L that can be deduced from experiments by fitting the curves $h_{stop}(\theta)$ and $h_{start}(\theta)$ for inclination angle $\theta \in [\delta_1, \delta_2]$ and $\theta \in [\delta_3, \delta_4]$, respectively. The parameters δ_i correspond to the limiting angles for which these measurements can be done. As an example, for an inclination angle of the plane $\theta = \delta_1$, the static thickness h_{stop} diverges and for $\theta = \delta_2$, there is no deposit left on the plane, i.e., $h_{stop} = 0$. We use here $\delta_1 = 22^\circ$, $\delta_2 = 34^\circ$, $\delta_3 = 23^\circ$, $\delta_4 = 36^\circ$, and $L = 8 \times 10^{-4}$ m which are characteristic values of the parameters determined in the experiments of *Félix and Thomas* [2004]. With these parameters $h_{stop} = 2.6743 \times 10^{-3}$ m for $\theta = 25^\circ$ so that $h_{stop} \sim 7d$, where d is the typical grain diameter in the experiments and $h_{start} = 4.9767 \times 10^{-3}$ m with $h_{start} - h_{stop} \sim 6d$ ($h_{start}/h_{stop} = 1.861$).

[20] In the domain $\theta \in [\delta_1, \delta_2]$, the function h_{stop} has been shown to be an appropriate scaling parameter providing a

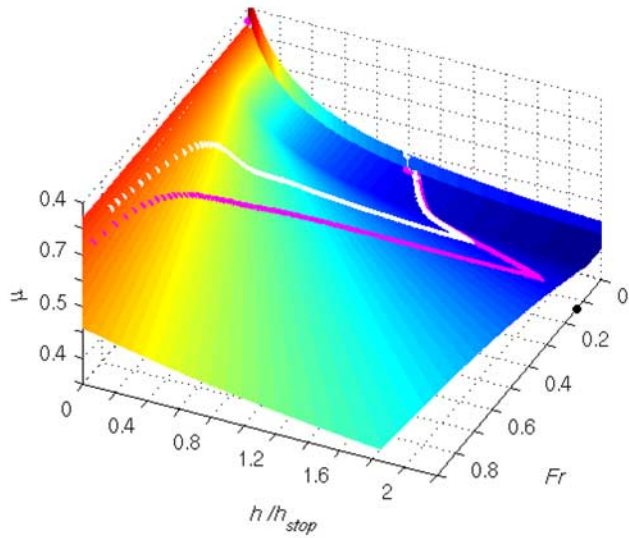


Figure 2. Friction coefficient defined by the empirical relation $\mu(h, Fr)$ (colored surface, equations (13)–(15)). The point $(Fr = \beta, h = 2.2, \mu = 0)$ has been represented in black in order to show the extension of the metastable regime $0 < Fr < \beta$. The colored lines represent the values of $(\mu(t), h(t)/h_{stop}, Fr(t))$ as time evolves at a fixed point A_1 ($x = 1.2$ m, $y = 0.1$ cm) situated at the middle of the plane, for the simulation of confined flow described in section 4 with a boundary flux $Q_1 = 2 \times 10^{-4} \text{ m}^2 \text{ s}^{-1}$ (white line) and $Q_2 = 4 \times 10^{-4} \text{ m}^2 \text{ s}^{-1}$ (magenta line).

relation between the thickness of the flow h and the Froude number $Fr = ||\mathbf{u}||/\sqrt{gh}$ for steady uniform flow

$$h_{stop} = \beta \frac{h}{Fr + \alpha} \quad (10)$$

whatever the size of the beads. The values of $\beta = 0.136$ and $\alpha = 0$ have been measured for glass beads ($\beta = 0.65$ and $\alpha = 0.136$ is found for sand particles) [Forterre and Pouliquen, 2003]. We use here the parameters measured for glass beads, typical of the material used in the experiments of Félix and Thomas [2004]. Relation (10) is defined when steady flow is possible, i.e., when $h > h_{stop}$ or equivalently when $Fr > \beta$.

[21] In steady uniform flows ($Fr > \beta$), the friction coefficient μ is related to the slope angle θ owing to the relation (6). Using (8) and (6), the friction coefficient can be expressed as a function of h_{stop}

$$\mu = \mu_{stop}(h_{stop}) = \tan \delta_1 + (\tan \delta_2 - \tan \delta_1) \frac{1}{\frac{h_{stop}}{L} + 1}. \quad (11)$$

Owing to relation (10), μ can be related to the thickness h and the Froude number Fr of the flow. On the other hand, for a uniform granular layer of thickness $h = h_{start}$, initially at rest ($Fr = 0$) on a plane with inclination, equations (6) and (9) give

$$\mu = \mu_{start}(h_{start}) = \tan \delta_3 + (\tan \delta_4 - \tan \delta_3) \frac{1}{\frac{h_{start}}{L} + 1}. \quad (12)$$

The behavior at $0 < Fr \leq \beta$ corresponds to metastable conditions, for which no measurements were available until very recently. An empirical ad hoc fit has been proposed by Pouliquen and Forterre [2002] to relate the behavior at $Fr > \beta$ to the measurements at $Fr = 0$ corresponding to destabilization from rest. Note that recent studies have been performed by Da Cruz [2004] providing insight into the flow law at small Froude numbers, i.e., $0 < Fr \leq \beta$.

[22] To sum up, the empirical friction coefficient $\mu(h, Fr)$ proposed by Pouliquen and Forterre [2002] and used here is defined as

if $Fr > \beta$

$$\mu(h, Fr) = \tan \delta_1 + (\tan \delta_2 - \tan \delta_1) \frac{1}{\frac{\beta h}{Fr L} + 1}, \quad (13)$$

if $Fr = 0$

$$\mu(h, Fr) = \tan \delta_3 + (\tan \delta_4 - \tan \delta_3) \frac{1}{\frac{h}{L} + 1}, \quad (14)$$

if $0 \leq Fr < \beta$

$$\mu(h, Fr) = \mu_{start}(h) + \left(\frac{Fr}{\beta}\right)^\xi (\mu_{stop}(h) - \mu_{start}(h)), \quad (15)$$

where ξ is a small parameter (here $\xi = 10^{-3}$). The colored surface represented in Figure 2 shows that for $Fr > \beta$ the coefficient of friction μ increases when the Froude number increases and when h decreases. For a given value of h , the coefficient of friction is almost constant in the metastable regime $0 \leq Fr < \beta$ and sharply increases near $Fr = 0$.

[23] The friction is then modeled by equation (7) with a variable Coulomb threshold $\sigma_c = gc\mu(h, Fr)$ with μ defined just above by equations (13)–(15). The friction model allows a mass initially at rest to flow when the driving forces due to surface slope and gravity exceed the Coulomb threshold related to μ_{start} . Similarly, the mass stops when the driving forces due to inertia, surface slope and gravity drop below the Coulomb threshold related to μ_{stop} . The model is therefore able to describe the hysteretic behavior of granular flows. In the case studied here, the “static” and “dynamic” friction coefficients are in the range $\mu_{start} \in [0.42, 0.73]$ and $\mu_{stop} \in [0.40, 0.67]$ respectively. Note that the flow law used here does not describe a constant value of the basal stress as proposed by Dade and Huppert [1998] or Kelfoun and Druitt [2005] but rather a constant friction coefficient in steady state owing to relation (6).

3.3. Numerical Method

[24] The numerical method used to solve the hyperbolic system (2)–(4) and (7) relies on a finite volume formulation together with the hydrostatic reconstruction scheme developed by Audusse et al. [2004] for Saint Venant models, and on the apparent topography approach of Bouchut [2004] to deal with friction. This numerical model has recently been successfully applied to the simulation of the collapse of a granular column over a horizontal plane by Mangeney-Castelnau et al. [2005]. This finite volume scheme provides second-order accuracy, in contrast with the first-order method

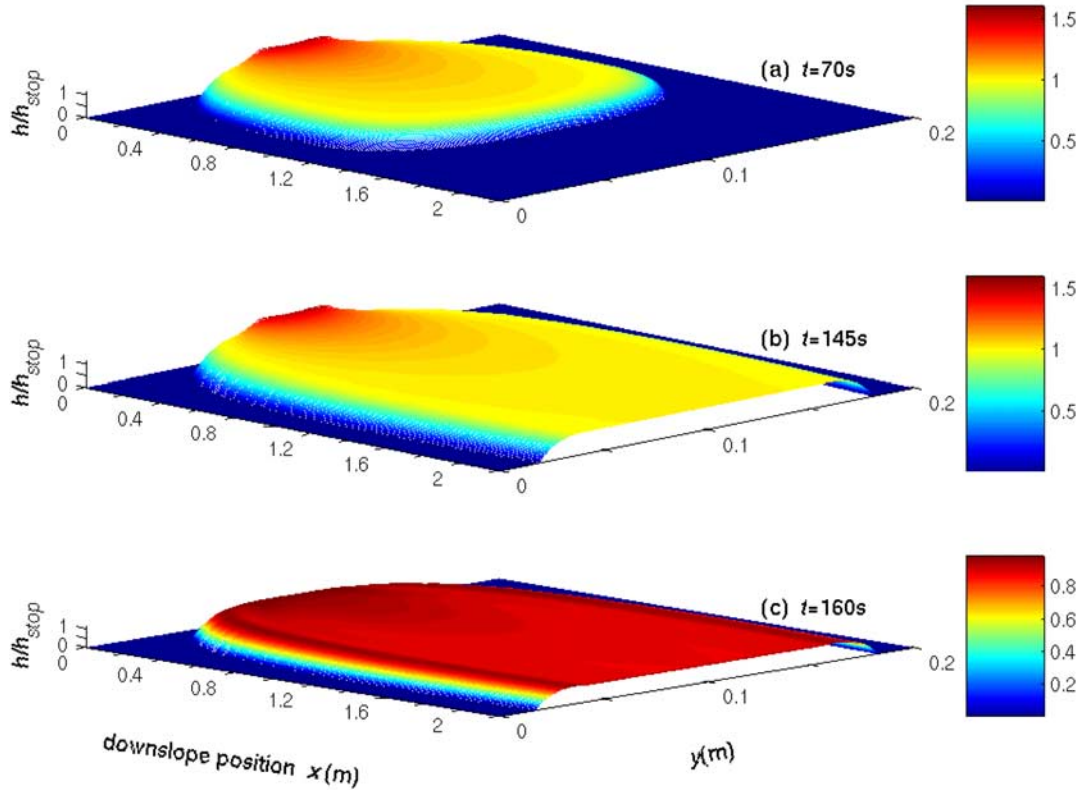


Figure 3. Numerical simulation showing (a, b) the creation of a self-channeling flow and (c) the formation of levee-channel morphology.

used by Mangeney-Castelnau *et al.* [2003] and based on a kinetic scheme. The method used is described in more detail in Appendix B and in the work by Bouchut [2004].

[25] Alternative methods have recently been proposed by Denlinger and Iverson [2004], based on a combination of finite volume and finite element schemes, and by Pitman *et al.* [2003], based on a finite volume scheme together with an adaptive grid. A comparison of these different methods would be of interest but is beyond the scope of this paper.

[26] For our purpose, we performed a series of numerical experiments on a two-dimensional regular grid with 400×100 points for the simulation of confined flows (section 4) and 400×300 points for unconfined flows (sections 5 and 6). At the upper boundary of the numerical model a flux and a thickness are imposed while free boundary conditions are prescribed on the other boundaries of the domain (Figures 3a and 3b). The stopping of the supply is imposed numerically by prescribing a zero flux and thickness at the left boundary of the domain (Figure 3c).

4. Simulation of Confined Flow

[27] To test the numerical model proposed here and to obtain an idea of its behavior, we will first simulate a case much simpler than that of unconfined flow: the confined flow of a transversally uniform layer of granular material over an inclined plane with a constant supply all across the plane in its upper part. This laboratory experiment, first performed by Pouliquen [1999], is the basis of the friction law presented

above. Numerical simulations using this empirical friction law have been shown to be able to reproduce granular behavior in unsteady situations [Pouliquen and Forterre, 2002; Mangeney-Castelnau *et al.*, 2003]. As in the work of Mangeney-Castelnau *et al.* [2003], with a numerical model based on a first-order kinetic scheme, the ability of the model to reach the right steady state and to calculate the thickness $h = h_{stop}$ once the supply is stopped is investigated here. Furthermore, the behavior of this flow and its stopping after the supply is shutdown gives a comparison tool when simulating the more complex case of free boundary channeling flow.

[28] Two numerical experiments are performed by imposing at the upper boundary, over the full width of a plane with an inclination angle $\theta = 25^\circ$: (1) a flux $Q_1 = hu = 2.10^{-4} \text{ m}^2 \text{ s}^{-1}$ (Figures 4a and 4c) and (2) a flux $Q_2 = hu = 4.10^{-4} \text{ m}^2 \text{ s}^{-1}$ (Figures 4b and 4d). Wall boundary conditions are imposed on the lateral part of the numerical domain. The numerical domain is $L_x = 2.2 \text{ m}$ long and $L_y = 20 \text{ cm}$ wide. The supply is kept constant until a steady uniform regime is reached. Then, the supply is stopped at $t_s = 70 \text{ s}$ and $t_s = 60 \text{ s}$ in the simulation with the input flux Q_1 and Q_2 , respectively. Finally, the final thickness of the deposit on the inclined plane is measured.

4.1. Evolution to Steady State

[29] Numerical results show that, using the flow law (13)–(15), the flow actually reaches a steady state (Figures 4a and 4b). The thickness being normalized by h_{stop} , a natural

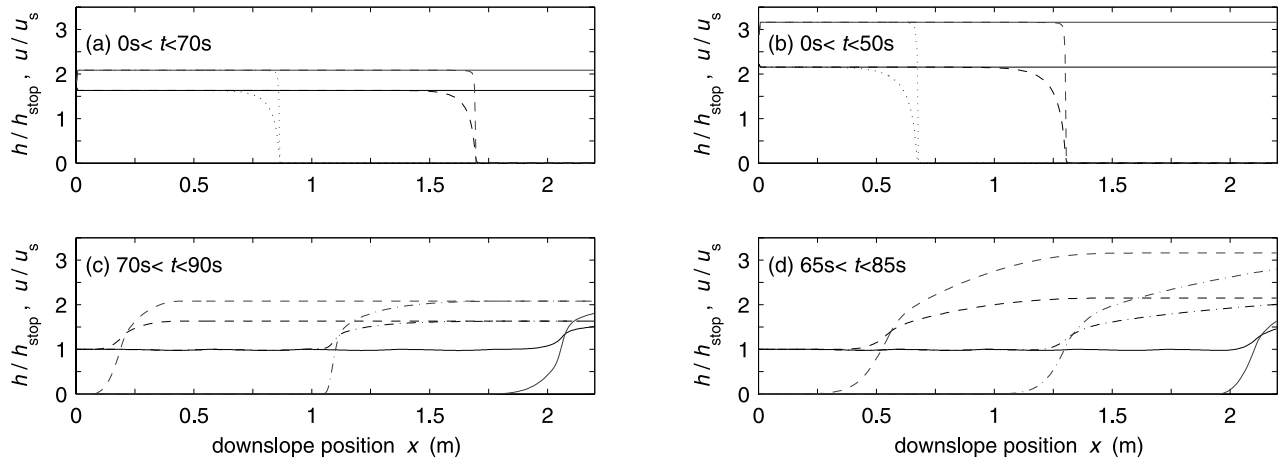


Figure 4. Evolution of the downslope profiles of the normalized thickness $h(x)/h_{stop}$ (black lines) and of the velocity of the lobe $u(x)/u_s$ (gray lines) at $y = 10$ cm, i.e., center of the flow, during the granular flow created by (left) the input flux $Q_1 = 2 \times 10^{-4} \text{ m}^2 \text{ s}^{-1}$ and (right) the input flux $Q_2 = 4 \times 10^{-4} \text{ m}^2 \text{ s}^{-1}$. Profiles are under constant supply at (a) $t = 10$ s (dotted lines), $t = 30$ s (dashed lines), and $t = 50$ s (solid lines) and (b) $t = 10$ s (dotted lines), $t = 30$ s (dashed lines), and $t = 50$ s (solid lines) and are shown during the draining phase at (c) $t = 72$ s (dashed lines), $t = 81$ s (dash-dotted lines), and $t = 90$ s (solid lines), and (d) $t = 66$ s (dashed lines), $t = 74$ s (dash-dotted lines), and $t = 82$ s (solid lines).

choice to normalize velocities is $u_s = \beta \sqrt{gh_{stop}} = 0.022 \text{ m s}^{-1}$ owing to relation (10). The characteristic velocity u_s is proportional to the gravity wave velocity in shallow flows $\tilde{c} = \sqrt{gh \cos \theta}$ ($u_s \simeq \beta \tilde{c}$ here). In the first experiment with an input flux $Q_1 = 2 \times 10^{-4} \text{ m}^2 \text{ s}^{-1}$, the steady state velocity of the flowing material is $u_1 = 2.08 u_s = 4.58 \times 10^{-2} \text{ m s}^{-1}$ and the steady state thickness is $h_1 = 1.63 h_{stop} = 4.36 \times 10^{-3} \text{ m}$ (Figure 4a).

[30] The values (h, u) , i.e., the steady thickness and velocity, corresponding to a given input flux can be calculated without any numerical simulation owing to relation (10). In fact, this equation can be written as

$$u = \gamma h^{\frac{3}{5}} \quad (16)$$

with $\gamma = \beta \sqrt{g}/h_{stop}$. The flux is defined as $Q = h u$, making it possible to calculate

$$h = \left(\frac{Q}{\gamma} \right)^{\frac{5}{8}} \quad (17)$$

and

$$u = \gamma^{\frac{2}{5}} Q^{\frac{3}{8}}. \quad (18)$$

[31] Equations (17) and (18) give exactly the values (h_1, u_1) calculated above in the case of an input flux $Q_1 = 2 \times 10^{-4} \text{ m}^2 \text{ s}^{-1}$, confirming the validity of the model. Interestingly, the numerical model makes it possible to satisfy the relation (10) in steady uniform regime although it is only weakly imposed. Note that, this relation does not hold in unsteady non uniform regime as near the front as will be discussed in section 6.2.1. In the second experiment where the input flux is two times greater: $Q_2 = 4 \times 10^{-4} \text{ m}^2 \text{ s}^{-1}$, the steady thickness and velocity are $h_2 = 2.15 h_{stop} \simeq 1.3 h_1$ and $u_2 = 3.16 u_s \simeq 1.5 u_1$ respectively (Figure 4b). In both

experiments, the front velocity rapidly reaches a constant value. The steady state front velocity is $v_{f2} = 6.3 \times 10^{-2} \text{ m s}^{-1} > v_{f1} = 4.1 \times 10^{-2} \text{ m s}^{-1}$ while the wave velocities are $\tilde{c}_2 = 0.23 \text{ m s}^{-1}$ and $\tilde{c}_1 = 0.20 \text{ m s}^{-1}$. Note that the front velocity is slightly smaller than the steady state mean velocity of the flow.

[32] Let us look at the role of the forces involved in equations (3)–(4), represented here by their corresponding accelerations normalized by the acceleration due to gravity g (hereafter called force) and defined as the inertial force

$$\mathbf{f}_i = \frac{1}{g} \left(\frac{\partial u}{\partial t} + cu \frac{\partial u}{\partial x} + v \frac{\partial u}{\partial y}, \frac{\partial v}{\partial t} + cv \frac{\partial v}{\partial x} + u \frac{\partial v}{\partial y} \right), \quad (19)$$

the force of gravity

$$\mathbf{f}_g = (-\sin \theta, 0), \quad (20)$$

the pressure force

$$\mathbf{f}_p = \left(-c \frac{\partial}{\partial x} (hc), -\frac{\partial}{\partial y} (hc) \right), \quad (21)$$

and the friction force

$$\mathbf{f}_f = \left(-\mu c \frac{u}{\|\mathbf{u}\|}, -\mu c \frac{v}{\|\mathbf{u}\|} \right). \quad (22)$$

[33] The forces represented in Figure 5 with a positive sign are driving forces whereas the forces with a negative sign are resisting forces. These forces have a component in the downslope direction X and a component in the transverse horizontal direction Y . In the steady state regime, reached after a given time, the friction force balances the force of gravity as is shown in Figure 5. This is true over the whole domain except near the supply, where the thickness

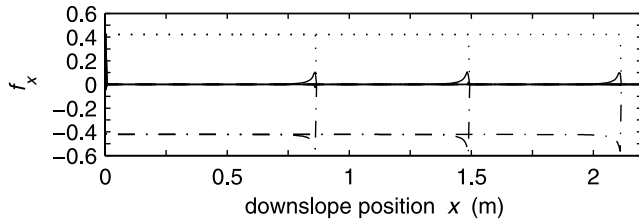


Figure 5. Normalized x components of the forces at times $t = 20$ s, $t = 30$ s, and $t = 40$ s: f_{px} (solid lines), f_{gx} (dotted lines), and f_{fx} (dash-dotted lines) as functions of the downslope position x . The force of inertia is negligible compared to the others and is not represented here.

decreases to reach the steady flowing thickness, and near the front where the pressure force related to the gradient of the free surface provides an additional driving force balanced by an increasing friction force. The friction force actually increases as the thickness decreases because of its explicit dependence on h according to relations (13)–(15). Although the dependence on h is very different for the pressure force (related to the gradient of the free surface $\partial h/\partial x$) compared to that of the friction force, these effects finally balance each other in order for the flow to reach a steady state. The acceleration and inertial forces are negligible here. In this case, the gradient of the free surface near the front and the increase of friction due to the small thickness provide a second-order balance compared to the first-order balance between the force of friction and gravity. However, this second-order balance may play a significant role in other configurations as will be discussed in section 6.

4.2. Stopping Phase

[34] Once the supply is cut, the stopping phase propagates downslope and leaves a deposit of thickness $h \simeq h_{stop}$ on the inclined plane for the two cases studied here (Figure 6). Although no experimental observations are available for this stopping phase, it is described here for the sake of comparison with further simulations of unconfined flows. The shape of the thickness and velocity at the rear of the stopping material changes with the input flux (Figures 4c and 4d).

[35] A 1-D wave generated by the stopping phase can be observed on the deposit shown in Figure 6 at a scale much smaller than the grain diameter. This oscillation is not present on the flowing free surface and is clearly related to the stopping phase. Whether or not this stopping wave is relevant for real granular flows is not really clear. However, one may ask what effect such a dynamic wave could have on real granular flows. In such a situation, some density waves would be expected within the material. A wavelength can be defined for the deposit thickness although it is not really constant. The wavelength of the deposit thickness oscillation is slightly smaller in the case of a flux $Q_2 = 2Q_1$ and does not depend on the number of grid points. However, the physical or numerical nature of this oscillation needs to be studied in more detail, which is beyond the scope of this paper.

4.3. Dynamic Path and Flow Law

[36] It is of interest to see which part of the flow law is investigated in this experiment. Figure 2 shows how the

values $(\mu(t), Fr(t), h(t)/h_{stop})$ change with time for $0 \leq t \leq t_s$. This so-called dynamic path is measured at the point A_1 ($x = 1.2$ m, $y = 10$ cm) located both in the center of the channel for the y direction and at the middle of the plane in the downslope direction. The white and magenta lines represent the dynamic path in the first experiment ($Q_1 = 2 \times 10^{-4} \text{ m}^2 \text{ s}^{-1}$) and in the second experiment ($Q_2 = 4 \times 10^{-4} \text{ m}^2 \text{ s}^{-1}$) respectively. In the first experiment, the granular front reaches A_1 at time $t \simeq 25$ s corresponding in Figure 2 to the beginning of the decrease of the Froude number at very small thicknesses. Then, the thickness increases with decreasing friction coefficient and decreasing Froude number until the steady state regime is reached, corresponding to the top of the hatpin shape for $h = h_1$ (white lines). The behavior of all the other points in the uniform part of the flow ($x > 80$ cm) follow the same path as point A_1 . In the second experiment ($Q_2 = 2Q_1$), the path of point A_1 is qualitatively the same and another steady state $h_2 > h_1$, $Fr_2 > Fr_1$ is reached. The friction coefficients μ obtained in the steady uniform regime are actually exactly equal to $\mu = \tan \theta = 0.4663$ in the first and second experiments as would be expected from equation (6). As a result, the value of μ in all steady uniform regimes, whatever the input flux and the related steady thickness and velocity, is equal to $\mu = \tan \theta = 0.4663$ as would be expected from equation (6). This strongly supports the validity of the numerical model used here. In regions where the flow is not uniform (i.e., near the front), equation (6) does not hold and the friction coefficient changes because the friction force balances the driving forces due to gravity and pressure gradients as shown in Figure 5.

[37] When the supply stops (at the top of the hatpin shape), the thickness strongly decreases with decreasing Froude number and increasing friction coefficient until the regime $Fr < \beta$ is reached. The path is then deviated and the thickness and the Froude number decrease with increasing μ until the stopping of the mass. The shape of the friction law at $Fr < \beta$ will completely determine the way of stopping and must be investigated using the new results provided by *Da Cruz* [2004]. Interestingly, after the supply is cut, the two paths almost collapse and the stopping phase is almost identical whatever the input flux Q , except precisely at the final stop.

5. Simulation of Unconfined Flow

5.1. Formation of Channel and Levees

[38] Let us now look at the more complex configuration of unconfined granular flows. The aim is to study the

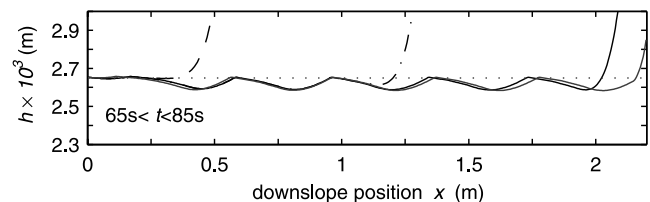


Figure 6. Thickness h in m within the vertical range $[h_{stop} - d, h_{stop} + d]$ during the granular flow created by the input flux $Q_2 = 4 \times 10^{-4} \text{ m}^2 \text{ s}^{-1}$ once the supply is cut at times $t = 66$ s (dashed lines), $t = 74$ s (dash-dotted lines), and $t = 82$ s (solid lines). The line $h = h_{stop}$ (dotted line) and the deposit obtained for the input flux Q_1 (gray line) have been added.

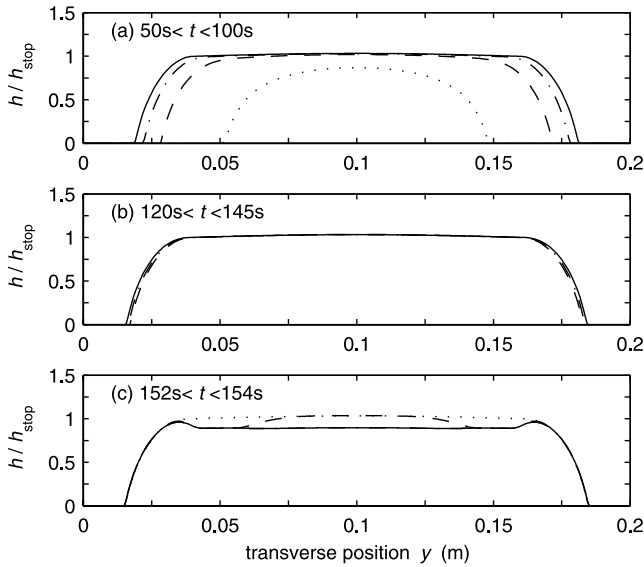


Figure 7. Transverse profiles $h(y)/h_{stop}$ at $x = 1.2$ m during the flow of the granular lobe (a) under constant supply at $t = 60$ s (dotted line), $t = 70$ s (dashed line), $t = 80$ s (dash-dotted line), and $t = 100$ s (solid line); (b) under constant supply at $t = 120$ s (dashed line), $t = 130$ s (dash-dotted line), and $t = 144$ s (solid line); and (c) during the draining phase at $t = 152$ s (dotted line), $t = 153$ s (dashed line), and $t = 154$ s (solid line).

channeling process as well as the formation of levee-channel morphology of the deposit. While a detailed comparison between numerical and experimental results would be of great interest, it is beyond the scope of this paper. We set the initial and boundary conditions in the range of the experimental conditions of *Félix and Thomas* [2004]: at the upper boundary, corresponding to the top of the inclined plane, a flux $Q_0 = hu = 2 \times 10^{-4} \text{ m}^2 \text{ s}^{-1}$ and a width $w_0 = 4$ cm are imposed generating a granular lobe flowing over a plane with inclination angle $\theta = 25^\circ$. These values give a flux $Q_0 = Q_0 w_0 = 8 \times 10^{-6} \text{ m}^3 \text{ s}^{-1}$, leading to a mass flux of 12 g.s^{-1} for glass beads of density $\rho = 2500 \text{ kg m}^{-3}$ and a mean density of packing $\phi \sim 0.6$, a typical value for dense granular materials. As in the simulation of confined flows, the numerical domain is $L_x = 2.2$ m long and $L_y = 20$ cm wide. The supply is stopped at $t_s = 145$ s and the total simulation lasts 160 s. At $t = 130$ s the front has already left the plane, leaving behind a flow quasi-uniform in the downslope direction for $x \geq 1.2$ m. At the right boundary of the domain, i.e., at the end of the plane, free boundary conditions are imposed (the x derivative of the thickness and velocity are set to zero).

[39] The building of shoulders channeling the flow and the appearance of levee-channel morphology in the deposits have been simulated numerically for the first time. The main achievement of these simulations has been to show that neither mixture concepts nor polydispersity are required to explain self-channeling flows and levee formation. The numerical simulation (Figure 7) shows the same evolution as in the experiments. The transverse profiles $h(y, t)$ obtained at a distance $x = 1.2$ m from the supply are in very good qualitative agreement with the experimental observations:

[40] 1. The front of the flow arrives at the chosen distance and the thickness and width of the cross section increase until an almost stable profile is reached (Figure 7a).

[41] 2. The profiles are globally stable with time although the width of the flow slightly increases (Figure 7b). When looking at the downslope velocity, two static shoulders occur at the left and right lateral borders of the flow (see section 6).

[42] 3. Finally, as the supply stops, the central part is drained by the downward flow and the thickness between the shoulders decreases. On the other hand, the thickness of the shoulders remains almost the same (Figure 7c).

[43] Note that the shapes of the flowing lobe and the levee-channel deposit are qualitatively similar to those observed by *Félix and Thomas* [2004] for almost monodisperse beads. When polydispersity is increased, the flowing lobe has a more rounded shape and the levees are more pronounced. A series of experiments involving monodisperse beads would be necessary to quantitatively compare numerical and experimental results.

[44] The front propagates and leaves behind a quasi-uniform thickness of material with a width w defined as the transverse extension of the granular mass as well as a quasi-uniform flowing width w_f defined as the width of material having a nonzero downslope velocity u . In this numerical experiment, the thickness of the granular mass is always lower than h_{start} ($h_{start}/h_{stop} = 1, 86$) as was the case for the same input flux in the case of confined flow studied in section 4. The maximum almost steady thickness of the flow at $x = 1.2$ m is $h_{s1} = 1.03 h_{stop} \simeq h_{stop}$. In the experiments, the flowing thickness is significantly higher than h_{stop} . This small calculated value of h may be explained by the absence of downslope shear stresses τ_{xy} . Friction is expected to be significant in the shear zones between the flowing material and the almost static shoulders; however, it is neglected in LWA models. The key role of sidewall friction on the flowing material for confined flows is well known and empirical relations based on experimental results have been proposed to take it into account [Roberts, 1965; Savage, 1979; Hutter and Koch, 1991; Taberlet et al., 2003; Jop et al., 2005]. In this relation, an additional friction force is added resulting from the presence of walls

$$\mu' = \mu + \mu_w \frac{h}{W}, \quad (23)$$

where μ_w is related to the friction between the wall and the flowing material and W is the width between the two walls. The shoulders can be considered here as walls confining the flow ($W = w_f$). However, shear stresses on planes orthogonal to the bed are expected to be significant also near the margins of the flow. Such stresses have been calculated rather simplistically by *Iverson and Denlinger* [2001] on the basis of an Earth pressure coefficient approach and assumptions concerning the orientation of principal stresses and more rigorously by *Denlinger and Iverson* [2004] using a finite element method that involved no such restrictions. In both cases, numerical results show that these shear stresses play an important role along the margins of flows. The modified friction force (23) or even better a rigorous description of the shear stresses normal to the bed would

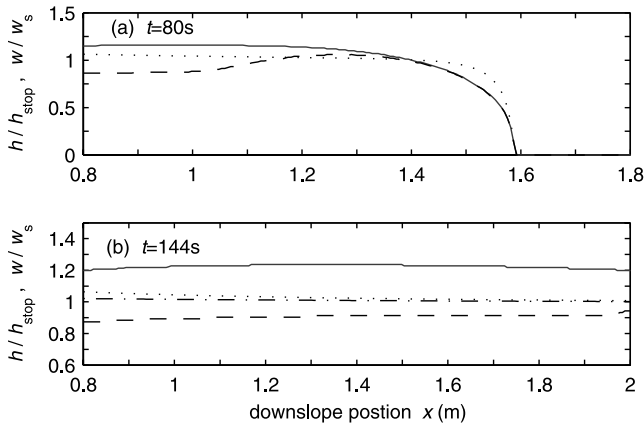


Figure 8. Downslope profiles of the total width $w(x)/w_s$ (solid gray lines), flowing width $w_f(x)/w_s$ (dashed lines), and thickness $h(x)/h_{stop}$ (dotted lines) at $y = 0.5L_y$, i.e., the center of the plane, during the flow of the granular lobe under constant supply at (a) $t = 80$ s and (b) $t = 144$ s. In Figure 8b the thickness $h(x)/h_{stop}$ at $y = 0.73L_y$ has been added as a dash-dotted line.

significantly improve the quantitative results provided by numerical simulations using LWA.

5.2. Relation Between Dynamics and Deposits

[45] Behind the front, the width and thickness of the flow increases upslope until reaching a quasi constant value (Figure 8a). Consequently a front zone can be defined, extending upslope between the front and the quasi-uniform flow situated at $x = x_r$. The position x_r is determined by the location where the flowing width w_f begins to be constant. Figure 8a shows that the extension of the front zone is $x_f - x_r \simeq 1.6 - 1 = 0.6$ m for these values of slope, flux, and rheological parameters. Near the front ($1.4 \text{ m} < x < 1.6 \text{ m}$, at $t = 80$ s) the width of the flowing central channel w_f is the same as the total width indicating that all the material in the front zone has a downslope velocity. At around 25 cm upward from the front, the width of the flowing material becomes smaller than the total width, marked by the appearance of two zones bordering the flow with no downslope velocities. These two regions defined by $\frac{w_f}{2} < |y - y_c| < \frac{w}{2}$ where $y_c = 0.1$ m is the center of the plane in the transverse direction, will be called shoulders hereafter. The thickness as well as the total and flowing widths of the lobe vary slightly with position. However, these variations are very small for $x \geq 1.2$ m, a distance for which the quasi permanent regime has been reached, at time $t = 144$ s, a time for which the front is far away, just before the supply stops (Figure 8b). For example, for $1.2 \text{ m} < x < 1.8 \text{ m}$ the thickness variation is $\Delta h/h \simeq -2\%$, the total width variation is $\Delta w/w = -2\%$, and the flowing width variation is $\Delta w_f/w_f = 1\%$. The flowing thickness h along the central axis of the plane ($y = L_y/2$) is stable over time but depends on the distance from the supply. When approaching the levees ($y = 0.73L_y$), this thickness is quasi-uniform as shown by the dash-dotted line in Figure 8b, because it is less sensitive to the thickness imposed as a boundary condition at the supply. The width of the lobe w changes slowly with time as is shown in Figure 9. Furthermore instabilities develop, leading to a spatial variation of w (Figures 10d

and 10e), which will be discussed in section 6.4. As a result, the measurement of the total width of the lobe in the field will be difficult to link to the mechanical properties of the granular material given that the measured width will depend on the duration of the event and on the location where the measurement is performed. On the contrary, the flowing width w_f is observed to very rapidly reach a quasi-uniform value (Figure 9). The width of the central channel of the deposit almost corresponds to the flowing width. Pertinent field measurements are the width and thickness of the central channel, far from the supply and far from the front, because they do not depend on the duration nor on the location where the field measurements are performed.

[46] Let us investigate, at a given downslope position x far from the supply and the front, the relation between the values, averaged over the width of the flowing channel w_f , of the thickness h_f and mean velocity u_f of the flowing material. Equation (16) obtained experimentally for uniform steady flow over an inclined plane confined between two walls gives

$$u_f = \gamma h_f^{3/2}. \quad (24)$$

[47] Let us assume that this relation is valid in the quasi uniform and steady part of the lobe. The validity of the relation (24) actually depends on the position along the plane and will be analyzed in detail in section 6.2.1. The flux of material at position x is $Q_f = Q_f w_f = h_f u_f w_f$ so that equation (24) reads

$$w_f = \frac{h_{stop}}{\beta \sqrt{g}} Q_f h_f^{-5/2}. \quad (25)$$

[48] A natural choice to normalize the width is then

$$w_s = \frac{h_{stop}}{\beta \sqrt{g}} Q_0 h_{stop}^{-5/2}, \quad (26)$$

where Q_0 is the flux at the supply defined in the previous section. In the following, the characteristic flowing width w_s will be used to normalize the calculated widths (Figures 8 and 9). Equations (25) and (26) give

$$\frac{w_f}{w_s} = \frac{Q_f}{Q_0} \left(\frac{h_f}{h_{stop}} \right)^{-5/2}. \quad (27)$$

Numerical results show that, once the flow is established, $Q_f/Q_0 \sim 1$, indicating a small exchange between the flowing material and the quasi-static shoulders. In the present simulation, at $x = 1.5$ m and $t = 144$ s, the calculated

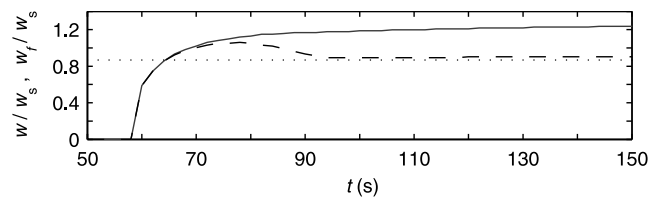


Figure 9. Change with time of the total width of the lobe $w(t)/w_s$ (solid gray lines) and of the flowing width $w_f(x)/w_s$ (dashed line) at $x = 1.2$ m. The width of the central channel w_c/w_s of the deposit has been added as a dotted line.

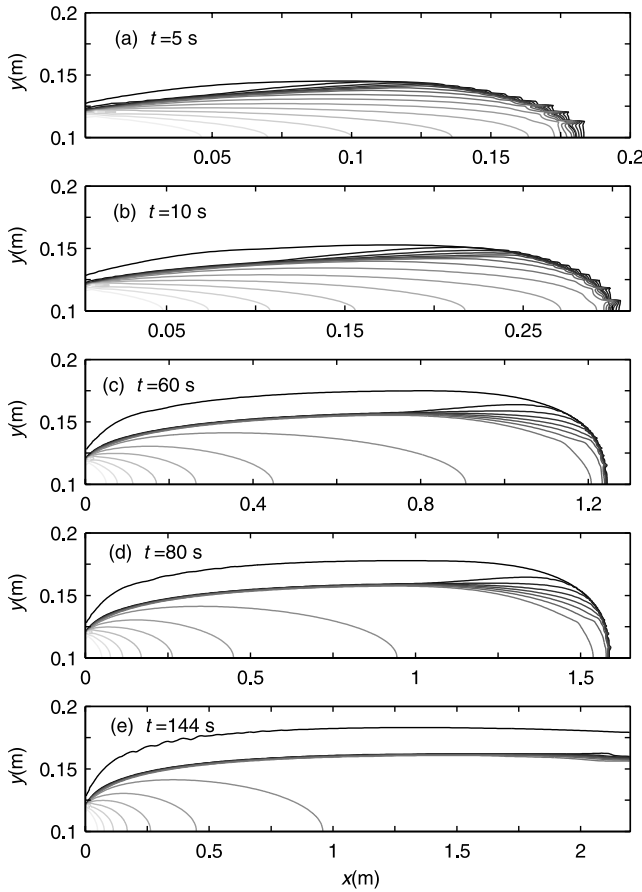


Figure 10. View from the top of half part ($y \geq L_y/2$) of the granular lobe showing change with time in the isovalues of the downslope velocity $u(x, y)/u_s$ as a function of the position in the plane (x, y) at several points in time t ; 15 isovalues have been represented in each plot with the darker corresponding to zero and the lighter to the maximum velocity equal to (a, b) $u_{max}/u_s = 1.92$ and (c–e) $u_{max}/u_s = 2.07$. The contour $h = 4.8 \times 10^{-4}$ m of the granular mass has been added in black.

normalized flowing width is $w_f/w_s = 0.90$ and the maximum normalized thickness is $h_f/h_{stop} = 1.03$ so that $(h_f/h_{stop})^{-5/2} = 0.93$. The relation

$$\frac{w_f}{w_s} = \left(\frac{h_f}{h_{stop}} \right)^{-5/2} \quad (28)$$

would therefore appear hold numerically. The numerical values suggest that the flux Q_f is slightly smaller than Q_0 , indicating a nonzero contribution of the transverse velocity to the total flux.

[49] Furthermore, the width of the central channel of the deposit w_c is almost equal to w_f as shown in Figure 9. As a result, provided (24) holds for the field granular material and relation $w_f(Q_0)$ is defined numerically or experimentally (or if w_s is known), and provided h_{stop} is known, the measurement of w_c in the field will provide a first-order estimation of the flowing thickness h and of the velocity u during emplacement via relations (28) and (24). A more precise investigation of the flow and deposit, especially concerning the validity of equation (24), will be presented in section 6.

5.3. Draining Phase

[50] When the supply stops, the draining of the central channel is also reproduced by the numerical simulation. The thickness staying on the plane in the central channel $h_c = 0.89 h_{stop}$ is slightly smaller than h_{stop} (Figure 7c), contrary to what was observed in the experiments of Félix and Thomas [2004] where $h_c \simeq h_{stop}$. However, $\Delta h = h_{stop} - h_c \simeq 3 \times 10^{-4} \text{ m} < d$, where d is the grain diameter. As was discussed in section 5.1, this numerical small thickness may be due to the absence of lateral shear stresses in LWA causing the expected strong dissipation between the flowing layer and the quasi-static shoulders to be neglected. The thickness profiles as well as the downslope velocity profiles during the draining phase have a steeper slope than the profiles obtained for confined flows in section 4. This observation should be related to the much smaller flux $Q_f = h_f u_f = 6.5 \times 10^{-5} \text{ m}^2 \text{ s}^{-1}$ involved here in the flowing channel. The similar behaviors during the stopping phase of confined and unconfined flow suggest that the shoulders behaves almost like a wall during the draining phase. The velocity of the stopping wave calculated from the results presented in Figure 11 is of the same order as the wave velocity in shallow flows \tilde{c} and slightly increases with time as was observed for confined flow (see section 4). The downslope oscillation observed numerically on the deposit of confined flows and shown in Figure 6 is not present in the case of unconfined flow (Figure 11b). The presence of shoulders may add a degree of freedom in the system compared to confining walls and then increase its ability to absorb shocks through the interaction between the shoulders and the stopping material. This interaction is clearly reflected in the deformation of the free surface at $t = 153 \text{ s}$ just after the supply is cut (Figure 12e).

[51] The change in the shape of the granular layer during draining (dashed line in Figure 7c) is in very good agreement with the experimental observations. However, the experimental draining stage lasts much longer. Numerically, the channel is completely drained in 2 s at $x = 1.2 \text{ m}$ (Figure 7c) while it lasts a few seconds longer in the

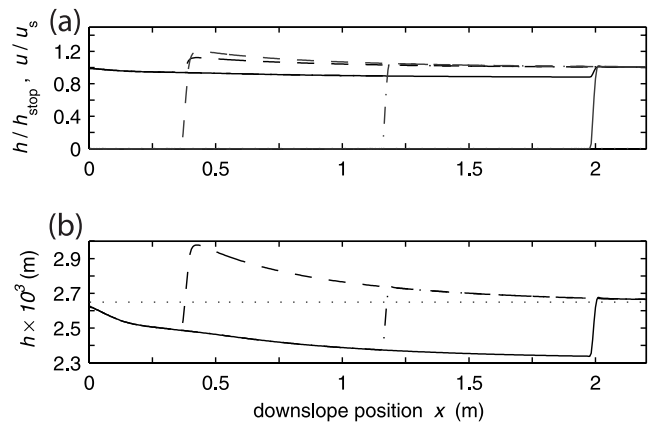


Figure 11. Downslope profiles of (a) the thickness $h(x)/h_{stop}$ (black lines) and downslope velocity $u(x)/u_s$ (gray lines) at $y = L_y/2$ during the draining phase at $t = 148 \text{ s}$ (dashed lines), $t = 153 \text{ s}$ (dash-dotted lines), and $t = 158 \text{ s}$ (solid lines) and (b) the thickness h within the vertical interval $[h_{stop} - d, h_{stop} + d]$. The line $h = h_{stop}$ has been added to Figure 10b as a dotted line.

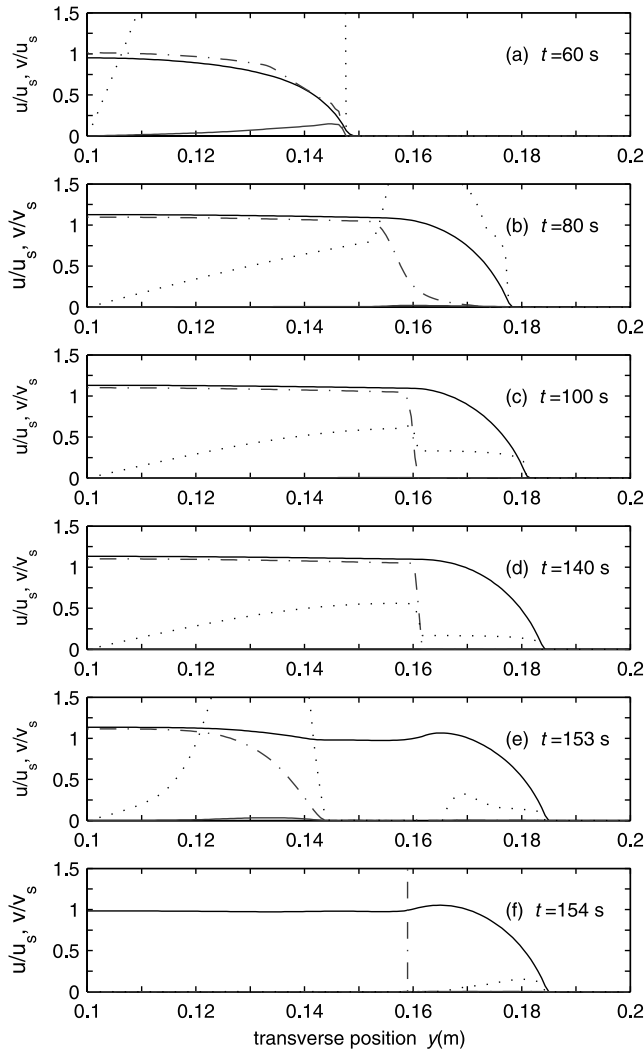


Figure 12. Downslope velocity $u(y)/u_s$ (dash-dotted gray lines) and transverse velocity $v(y)/u_s$ (solid gray lines) at $x = 1.2$ m as functions of the transverse position y for the half part of the lobe ($y \geq L_y/2$). The transverse profiles h/h_{stop} are represented by solid lines. Transverse profiles correspond to (a–d) a constant supply and (e, f) after cutting the supply at $t_s = 145$ s. The values of $100v$ have been added in dotted lines (the values $100u$ within the shoulders are too small to be visible). In Figure 12f the location used to calculate w_c is shown by a gray dash-dotted line.

experimental case. This observation is very similar to the result of the comparison between numerical and experimental results on the spreading of a granular column over a horizontal plane [Mangeney-Castelnau *et al.*, 2005]. The stopping phase was expected to be due to complex vertical propagation of the interface between static and flowing grains, which is not considered at all by our model.

6. Dynamics of Unconfined Flow

6.1. Several Flow Structures Within the Lobe

[52] The distribution of velocities makes it possible to shed light on the structure of the flow. From the very beginning, a front zone appears, creating two zones bordering the flow with very small downslope velocities. These

zones appear in Figures 10a–10d behind the front between the contour of the lobe and the darker isovalue of the horizontal velocity corresponding to $u = 0$. The flow creates its own channel by building lateral shoulders. With time, these zones spread laterally although the spreading slows with time. After $t = 100$ s, the flow structure is likely established. Once this state is reached, at any x , except near the front, there is a quasi-stationary state. The downslope velocity and thickness profiles are quasi-constant with time. Only the very slow widening prevents the state from being really stationary. The downslope velocity u is almost constant in the central part of the flow, and drops to 0 when moving transversally to the lateral borders (Figure 12). With time, the decrease to 0 becomes sharper, distinguishing two regions: a region with quasi-uniform flow directed downslope and a region of quasi-static lateral material slowly migrating in the transverse direction with no downslope component of the velocity. In Figures 12b–12f, the transverse velocity v is two orders of magnitude lower than the downslope velocity u . The values of $100v$ are represented by dotted lines in Figure 12. The slow transverse velocity v obtained numerically at $t = 100$ s and $t = 140$ s at $y > 0.16$ must be studied in more detail in order to assess their physical or numerical significance.

[53] Finally, when looking at Figures 10c, 10d, and 10e and at the y profiles of the downslope and transverse velocity u and v as time evolves (Figure 12), three distinct zones appear within the granular lobe: (1) a front zone where both horizontal and transverse velocities are present, (2) a quasi-uniform zone bounded by quasi-static shoulders, where the downslope velocity within the central part is almost constant while the transverse velocity is very small, and (3) a transition zone near the supply between boundary conditions and self-channeling flow where strong downslope gradients of the transverse and downslope velocity occur.

[54] The central flow is very similar to the confined flow studied in section 4, the lateral walls being replaced here by

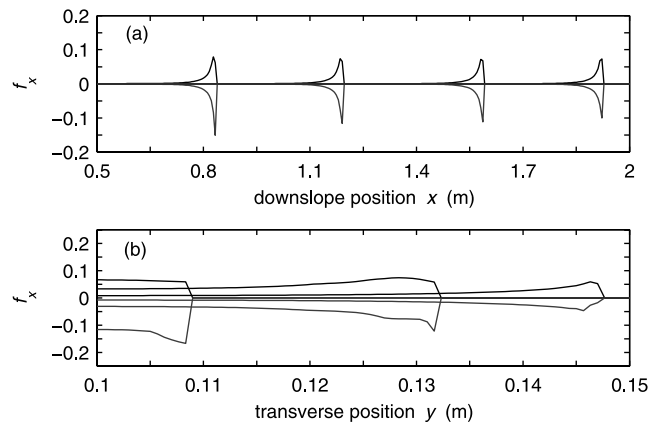


Figure 13. Normalized x component of the forces (see equations (20)–(22)) f_{px} (black lines) and $f_{fx} - f_{gx}$ (gray solid lines), as functions of (a) the downslope direction x at the center of the plane $y = L_y/2$, at times $t = 37$ s, $t = 57$ s, $t = 80$ s, and $t = 100$ s and (b) the transverse direction y at $x = 1.2$ m, at times $t = 57$ s, $t = 58$ s, and $t = 60$ s. Here $f_{px} > 0$ is a driving force and $f_{fx} - f_{gx} < 0$ is a resisting force.

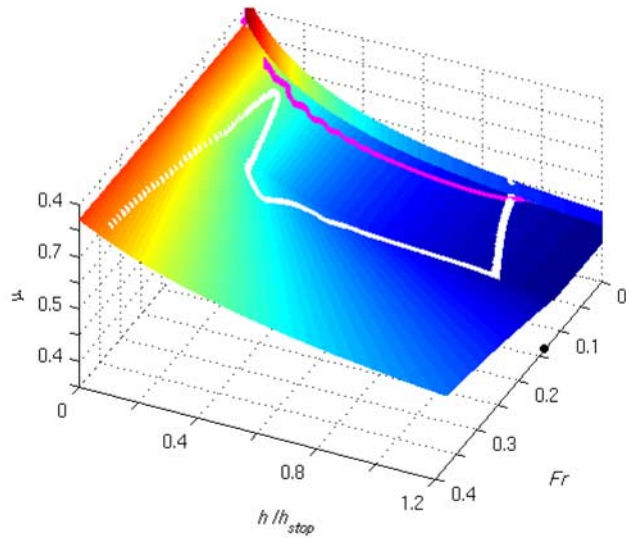


Figure 14. Friction coefficient defined by the empirical relation $\mu(h, Fr)$ (colored surface, equations (13)–(15)). The point ($Fr = \beta$, $h = 1.2$, $\mu = 0$) is represented in black in order to show the extension of the metastable conditions $0 < Fr < \beta$. The colored lines represent the values of $(\mu(t), h(t)/h_{stop}, Fr(t))$ as time changes at a fixed point: The white line represents the dynamic path at the point A_1 ($x = 1.2$ m, $y = L_y/2 = 0.1$ cm) in the central channel, and the magenta line refers to point A_2 within the shoulders ($x = 1.2$ m, $y = 0.165$ m).

quasi-static shoulders. Figure 13 shows the forces acting on the granular mass during the flow in the x direction as functions of x (Figure 13a) and as functions of y (Figure 13b). The pressure force is represented together with the difference between the friction force and the force of gravity. The inertial force is shown to be negligible in Figure 13 except at $t = 37$ s and $t = 57$ s where the deceleration $\partial u/\partial t$ is significant because of the high resisting force $f_{fx} - f_{gx}$ (gray line) compared to the driving pressure force f_{px} (black line). As for confined flow, at leading order, in the x direction, the friction force balances the force of gravity ($f_{fx} - f_{gx} = 0$) except at the front as shown in Figure 13a where the norm of the pressure force increases as does the difference between the friction force and the gravity force. Initially, the resisting friction force ($f_{fx} - f_{gx}$) is higher than the driving pressure force f_{px} as is the case at $t = 37$ s in Figure 13a at the front. With time, the forces at the front balance each other in order for the flow to reach a steady state (Figure 13a). A similar balance is observed within the granular lobe when representing the x component of the forces as a function of the y direction (Figure 13b). While the dissipation force is higher than the pressure force within the granular lobe at $t = 57$ s, these forces almost balance each other at $t = 60$ s (Figure 13b) although the flow just at the lateral margins is not perfectly solved numerically (see *Tai et al.* [2002] for more sophisticated numerical treatment of the margins). In our simple model, the second-order balance between the change of the friction force and the pressure force is shown to play a key role in the dynamics of the flow, making it possible to reach a steady state with nonuniform thickness. This balance would certainly change if the disregarded components of the stresses were accounted for.

6.2. Dynamic Path and Flow Law

6.2.1. Evolution to Steady State

[55] When looking at the dynamic path (Figure 14), the behavior is qualitatively similar to the confined case (Figure 2). The white lines describing the change of $(\mu(t), h(t)/h_{stop}, Fr(t))$ at a point A_1 situated within the central channel shows that when the thickness of the granular lobe begins to be significant, the friction coefficient decreases until a steady state is reached corresponding to the top of the hatpin shape. Once the supply is stopped, the thickness decreases until the material stops ($Fr = 0$).

[56] Figure 14 shows that, very rapidly, the Froude number is almost constant or decreases very slightly. As a result, numerical simulations show that the friction coefficient essentially depends on h . Note that the assumption of constant stress made by *Dade and Huppert* [1998] or *Kelfoun and Druitt* [2005], although not similar to the flow law (13)–(15), also implies a friction coefficient which depends on the thickness. Their assumption $|\tau_{xz}| = \mu g h = K$ leads to a linear decrease of μ as h decreases.

[57] The steady value of the friction coefficient $\mu = 0.4664$ is slightly higher than $\mu = \tan \theta$ obtained for the confined case. In fact, in the unconfined case, an additional small pressure force is involved in the equilibrium due to the small decrease of the thickness in the downslope direction. If we look at other positions within the plane, for example near the supply ($x = 5$ mm, $y = 0.1$ m) where

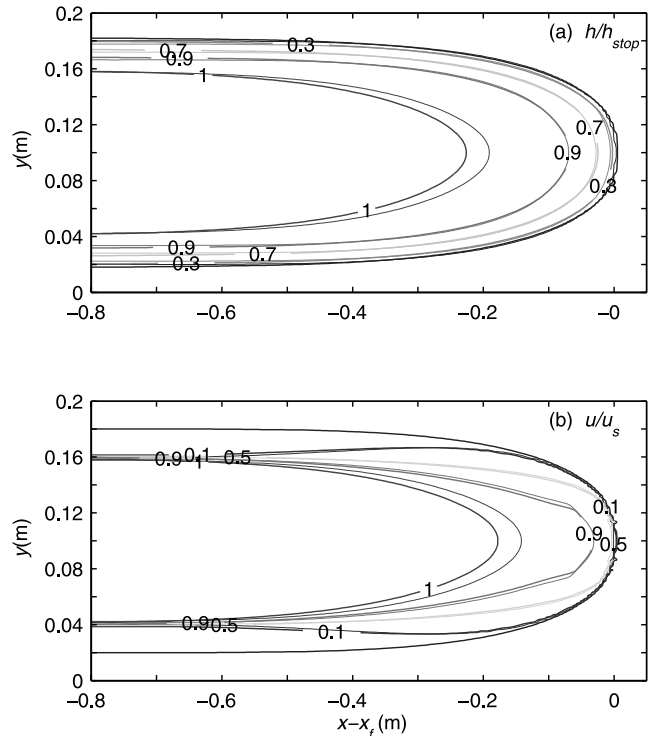


Figure 15. View from the top of the granular lobe near the front in a reference frame linked to the front ($x = x_f$). Shown are isovalues of (a) the normalized thickness h/h_{stop} and (b) the downslope normalized velocity u/u_s , represented at times $t = 90$ s (thin lines) and $t = 115$ s (thick lines). Thin and thick lines are almost superimposed, indicating the steady state reached by the front. The contour of the lobe at each time has been added in Figure 15b.

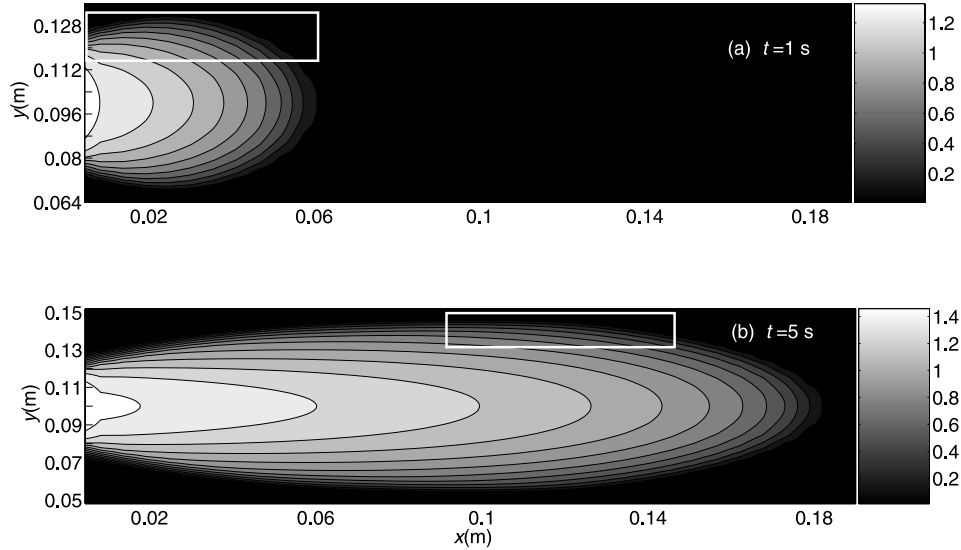


Figure 16. View from the top of the granular lobe near the front showing isovalues of the normalized thickness h/h_{stop} (a) at time $t = 1$ s and (b) at time $t = 5$ s. Zones in white rectangles are zoomed in Figure 17.

$\partial h / \partial x$ is higher, the calculated steady value of the friction coefficient is actually $\mu = 0.5678$, and on the contrary, at the end of the plane ($x = 2$ m, $y = 0.1$ m) where the thickness is almost constant downslope, the steady friction coefficient is $\mu = 0.4663$ which is exactly equal to $\tan 25^\circ$ as for the case of confined uniform flow studied in section 4.

[58] In the almost steady configuration, the relation (10) does not fully hold. In fact, when looking at the numerical results, we see that the relation between h and u depends on the forces involved at the point considered, and especially on the pressure force which was not taken into account when establishing relation (10). Small surface gradients could significantly change the proportionality factor β' relating h_{stop} to $\frac{h}{Fr}$

$$h_{stop} = \beta' \frac{h}{Fr}. \quad (29)$$

As a result, the calculated friction coefficient is different from that obtained in the uniform regime where $\partial h / \partial x = 0$ owing to relation (13). Actually, if relation (29) is obtained experimentally, it could result in a misleading interpretation such as the existence of a new value β' instead of the previous value of β which corresponds to the uniform regime in relation (10). The values of this meaningless factor β' could be deduced from the calculated steady value of the friction coefficient μ owing to (13) and (29) leading to

$$\mu = \tan \delta_1 + (\tan \delta_2 - \tan \delta_1) \frac{1}{\frac{\beta'}{\beta} \frac{h_{stop}}{L} + 1}. \quad (30)$$

Here for example, $\beta' = 0.137$ at $x = 73$ cm ($\mu = 0.46665$) and $\beta' = 0.697$ at $x = 5$ mm ($\mu = 0.5678$). If β is assumed to be constant in relation (10), measurements of the velocity could lead to an underestimation of the flowing thickness h ,

if this value is unknown. When interpreting experimental results, careful analysis is therefore required before concluding that relation (10) holds.

6.2.2. Metastable Regime

[59] The change with time of $(\mu(t), h(t)/h_{stop}, Fr(t))$ at a point A_2 situated within the shoulders (magenta line in

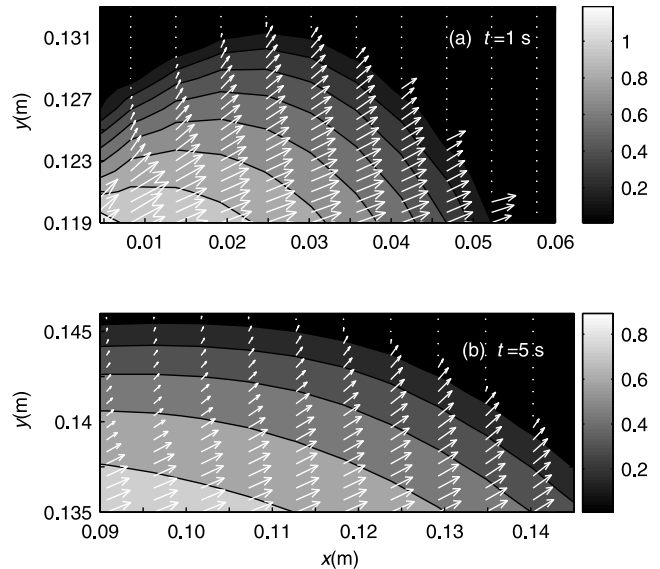


Figure 17. View from the top of particular zones defined in Figure 16 in the region of the granular front at times (a) $t = 1$ s and (b) $t = 5$ s. Isovalues of the normalized thickness h/h_{stop} are shown together with the velocity field \mathbf{u} represented by arrows. The lengths of the arrows are proportional to the norm of the velocity, showing its decrease when approaching the margins as well as the rotation of the velocity direction.

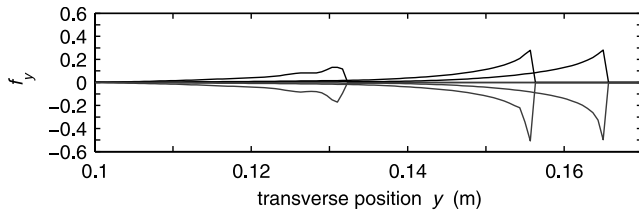


Figure 18. Normalized y components of the forces (see equations (20)–(22)): f_{py} (black solid lines) and f_{fy} (gray solid lines) as functions of the transverse direction y at $x = 1.2$ m and at times $t = 58$ s, $t = 62$ s, and $t = 66$ s. Here $f_{py} > 0$ is a driving force and $f_{fy} < 0$ is a resisting force. Note that the y component of the gravity f_{gy} is equal to zero.

Figure 14) is quite different from that at a point A_1 situated within the central channel (white line Figure 14). At the point A_1 , $Fr > \beta$ always holds. On the other hand, the dynamic path of point A_2 ($x = 1.2$ m, $y = 0.165$ m) shows naturally that flow within the levees is always in the metastable regime $0 < Fr < \beta$. Note that this part of the flow law has been determined ad hoc. The shape of the flow law in that regime will certainly greatly change the behavior and shape of the shoulders and levees. However, the dynamic path of point A_2 shows that the granular material never stops as long as the supply is maintained, as is observed experimentally [Deboeuf et al., 2006]. This suggests that the use of two friction angles, namely a static and a dynamic friction angle, is not necessary to explain the formation of self-channelling flows.

[60] The question is why and how this nearly steady self-channelling flow has been created.

6.3. Creation of the Shoulders Behind the Front

[61] After a certain time ($t > 60$ s in Figure 10), the structure of the front zone is clearly different from that of the flow behind. The front moves with a constant velocity after about 60 s when it is located at $x \geq 1.3$ m. The shape of the front and the velocity field within the front zone becomes also constant after around $t = 90$ s. Figure 15 represents a view from the top of the granular lobe. The isovalues of the normalized thickness (Figure 15a) and downslope velocity (Figure 15b) in a reference frame linked to the moving front at $t = 90$ s (thin lines) and $t = 115$ s (thick lines) shows that these isovalues, at the different times, are superimposed, reflecting the constant shape and velocity within the front zone in the reference frame moving with the front. With time, the front follows its own dynamics. Behind the front, quasi-uniform flow, slightly influenced by the supply, is established.

[62] The shape of the front seems to be responsible for the selected width of the granular lobe. The creation of shoulders at the rear of the front results from a strong rotation of the velocity as shown in Figures 16 and 17 representing two zones behind the front (white rectangles in Figure 16) on which it was zoomed in (Figure 17). At the very beginning, at $t = 1$ s and $t = 5$ s the velocity at the front is almost constant and mainly directed downslope (Figure 17). When moving upward from the front, at a given x position the velocity decreases transversally when approaching the lat-

eral borders and switches from the downslope x direction toward the transverse y direction (Figure 17). This rotation is also observed at $t > 90$ s when the front has been established,

[63] What makes the velocity decrease and rotate when approaching the lateral border of the lobe? In the vicinity of the front, at $t = 57$ s, the forces acting in the y direction are almost zero so that the velocity is mainly directed downslope. Figure 13b shows that the x component of the pressure force f_{px} is almost constant transversally at $t = 57$ s. The force of gravity is obviously also constant in the x direction. On the other hand, the friction is higher when approaching the shoulders because of small thickness. As a result, the downslope velocity u decreases when approaching the lateral border of the lobe. Upward from the front (at $t = 58$ s in Figure 13b), but still in the front zone, the same trend can be observed but the x pressure force f_{px} also increases transversally because of the shape of the front. However, the effect of increasing friction overweighs the driving effect of the pressure force and the balance of forces also leads to a deceleration of the downslope velocity when approaching the borders. Obviously, the y component of the friction force f_{fy} also increases because of small thickness when approaching the borders (Figure 18). The y component of the gravity force f_{gy} is equal to zero, inertia is negligible and the driving force is only the pressure force (black lines in Figure 18). As already observed in the x direction, the increase of dissipation due to friction overweighs the increase of driving effects due to surface gradient $\partial h / \partial y$ when approaching the lateral margins and the transverse velocity decreases ($\partial v / \partial t < 0$). However, the deceleration in the downslope direction because of the higher driving force f_{py} than that in the x direction ($|\partial h / \partial y| > |\partial h / \partial x|$) near the margins. The total velocity therefore rotates toward the transverse direction and decreases with time when approaching the lateral borders of the flow (Figure 17). In our simple model, the increase of the friction with decreasing thickness may then be the process responsible for the creation of shoulders bordering the flow. The complex competition between the pressure force and the friction when the thickness decreases seems to be a key mechanism controlling the dynamics of the front.

[64] However, would it really be necessary to include variable bed friction to produce the force competition that creates lateral levees if the disregarded components of the stress tensor were introduced in the model? In fact, at least in the SH-type approach, taking into account the anisotropy of normal stresses would add a multiplying coefficient k in the h gradient term that depends on the sign of the space gradient of the velocity field. On the other hand, following the approach proposed by Iverson and Denlinger [2001], the shear stresses on planes normal to the bed would introduce an additional term related to the y derivative of the thickness h in the x momentum equation and an additional term related to the x derivative of the thickness h in the y momentum equation. These terms would completely change the balance of forces. In the case of the SH theory, the creation of quasi-static zones could be explained in a different way. In fact, the equilibrium in the y direction behind the front involves a driving force related to the

h gradient in the y direction (pressure force), a lateral dissipation force related to the shear stress τ_{xy} involving the h gradient in the x direction and the so-called friction force. When moving from the center ($y = 0$) to the lateral border ($y = w/2$) at a given position x behind the front, the pressure force increases because of decreasing thickness, the friction force is constant because the friction coefficient μ is constant, and the lateral dissipation force increases because $\partial h/\partial x$ decreases behind the front when moving toward the lateral borders. This analysis suggests a possible relation between the μ parameterization and the neglecting of stresses on planes normal to the bed.

6.4. Instabilities

[65] Instabilities are observed near the supply as shown in Figure 10e. Instabilities in the lateral part of unconfined flow have also been observed in the experiments of *Deboeuf* [2005]. Note that this phenomenon was obtained numerically using a totally different code based on a kinetic scheme and finite volume elements with an unstructured grid as described by *Mangeney-Castelnau et al.* [2003]. However, more investigations must be carried out in order to be sure that these instabilities are not of a numerical nature. Some oscillations are also observed near the front but seem to be related to the discretization.

[66] The region near the supply is subjected to strong gradients of the velocity field due to the transition between boundary conditions and the developed flow along the plane. After a few tens of seconds, near the supply, the width of the lobe increases regularly until $x \simeq 20$ cm and stabilizes for larger values of x . An instability occurs at this transition. One explanation could be that the expansion of the granular mass near the supply is blocked by quasi-static shoulders and the material is only allowed to flow in the downslope direction. The change of direction from expansion to downslope motion may be at the origin of the initiation of the instability observed in this region. Instability can also be observed on the dynamic path of the points situated within the shoulders (Figure 14). As the thickness of the shoulders increases after the front has passed the friction decreases while the Froude number oscillates.

7. Conclusion

[67] It has been shown here that numerical simulation using the Saint Venant approach with the empirical variable friction law proposed by *Pouliquen and Forterre* [2002] makes it possible to simulate the complex behavior of unconfined flow. The creation of a channel with a given width as well as the separation of the flow between an inner quasi-steady regime in the downslope direction together with quasi-static borders is surprisingly well reproduced. The major achievement of these simulations has been to show that neither mixture concepts nor polydispersity are needed to explain self-channelling flows and levee formation.

[68] The simulation have been performed using a parameterization of the coefficient of friction that depends on the thickness and the Froude number of the flow. The model is based on strong assumptions such as the isotropy of normal stresses and the neglecting of shear stresses on planes normal to the bed. These assumptions are expected to affect the interpretation of the results in the case studied here

where quasi-static zones develop near the lateral margins and where h gradients can be large. In particular, the absence of lateral dissipation between the flowing mass and the quasi-static shoulders likely leads to underestimation of the flowing thickness and the thickness of the deposit in the central channel. Furthermore, *Pouliquen and Forterre's* [2002] empirical flow rule is obviously oversimplified to describe the behavior of the complex geological materials involved in natural avalanches.

[69] Numerical results provide a possible explanation of the self-channelling process indicating that the shoulders are created behind the front. The fact that the front reaches a steady velocity and shape along the plane seems to be responsible of the width chosen by the flow. In the simplified model used here, the formation of shoulders channeling the flow has been shown to result from the balance between a friction force with a friction coefficient depending on the thickness of the flow and the driving forces due to gravity and surface slope. The competition between these forces leads to rotation of the velocity vector from the downslope direction within the central channel to the transverse direction when approaching the lateral border of the flow. The complex competition between the pressure force and the friction when the thickness decreases seems to be a key mechanism controlling the dynamics of the front. The balance of forces would be different if stresses on planes normal to the bed were taken into account. In that case, the increasing dissipation near the lateral borders behind the front would be expected to be due to the increasing downslope gradient of the thickness when moving from the center of the lobe toward the lateral margins. Simulation of self-channelling flows and analysis of the balance of forces using more sophisticated models such as the one proposed by *Denlinger and Iverson* [2004] would provide insight into the role of the different components of the stress tensor in the creation of quasi-static zones. Furthermore, it could be a way to understand the basis of the μ parameterization.

[70] The steady regime obtained in the central channel appears to be very similar to that observed on uniform laterally confined flows. The calculated flow within the central channel almost reaches a steady state with a constant value of the thickness and velocity at a given position. We have investigated the variation of the friction coefficient during the flow. The nonuniformity in space involving surface gradients locally modifies the steady coefficient of friction calculated by the numerical model, which appears to be slightly different from the case of steady uniform confined flow ($\mu = \tan \theta$). The dependence on the velocity of the friction coefficient appears to be weak. In fact, once the flow has developed, the Froude number is almost constant because the velocity varies like the wave velocity in shallow flow. The metastable regime is thoroughly investigated by the flow near the developing quasi-static margins. The accurate description of this regime is therefore essential when modeling the dynamics of these zones and the shape of the levees. However, in the case of our model, the granular material never stops as long as the supply is maintained as observed experimentally [*Deboeuf et al.*, 2006]. This suggests that the use of two friction angles, namely a static and a dynamic friction angle, is not necessary to explain self-channelling flows.

[71] The width of the flowing channel w_f has been proved to be almost constant in time and space. The width of the central channel on the deposit w_c almost corresponds to w_f and therefore provides a pertinent parameter for field measurements. Furthermore, the thickness in the central channel of the deposit h_c almost corresponds to h_{stop} , a parameter containing information on the mechanical properties of the granular mass. If the relation between the flowing width and the initial flux $w_f(Q_0)$ has been determined experimentally or numerically, the measurements on the field of the two parameters (h_c , w_c) would allow estimation of the thickness and velocity of the flow during emplacement. For pyroclastic flows, it would allow estimation of the flux of material emitted by the volcano. The detailed study of geomorphologic features observed on deposits of gravitational flows has been shown to provide a useful tool for the comparison of model and field observations and sheds new light on the flow law governing the motion of these complex granular flows.

Appendix A

[72] This appendix presents the new model used, which takes into account the curvature tensor

$$\mathcal{H} = c^3 \begin{pmatrix} \frac{\partial^2 b}{\partial x^2} & \frac{\partial^2 b}{\partial x \partial y} \\ \frac{\partial^2 b}{\partial x \partial y} & \frac{\partial^2 b}{\partial y^2} \end{pmatrix} \quad (\text{A1})$$

with all its components [Bouchut and Westdickenberg, 2004], although these components are equal to zero in the simple case studied here. In one dimension, our formulation can be reduced to the equations developed in former studies. The flow is described by

$$h(t, \mathbf{x}) \geq 0, \quad \mathbf{u}'(t, \mathbf{x}) \in \mathbb{R}^2, \quad (\text{A2})$$

where h is the thickness of the material layer in the direction normal to the topography, and $\mathbf{u}' = (u, u_t)$ (where the subscript t stands for transverse) is a parameterization of the velocity. This parameterization has been defined in order to simplify the equations when a 1-D topography $b = b(x)$ is considered. The real 3-D material velocity has horizontal/vertical components

$$\vec{\mathbf{u}} = (c\mathbf{u}', \mathbf{s} \cdot \mathbf{u}'). \quad (\text{A3})$$

This physical velocity is tangent to the topography, $\vec{\mathbf{u}} \cdot \vec{\mathbf{u}} = 0$, as would be expected for shallow flows and can be expressed as a 2-D vector $\mathbf{u} = (u, v)$ in the (X, Y) plane (Figure 1). In one dimension, \mathbf{u}' is actually the real scalar velocity u in the plane tangent to the topography. In the case simulated below dealing with the flow over an inclined plane with slope in the x direction, the real physical velocity \mathbf{u} has coordinates in the tangent plane given by

$$(u, v) = (u, cu_t). \quad (\text{A4})$$

[73] In the horizontal Cartesian coordinate formulation, the model can be expressed as (see (2.54)–(2.55) in work by Bouchut and Westdickenberg [2004])

$$\partial_t(h/c) + \nabla_{\mathbf{x}} \cdot (h\mathbf{u}') = 0 \quad (\text{A5})$$

$$\begin{aligned} \partial_t \mathbf{u}' + c\mathbf{u}' \cdot \nabla_{\mathbf{x}} \mathbf{u}' + \frac{1}{c}(\text{Id} - \mathbf{s}\mathbf{s}') \nabla_{\mathbf{x}}(g(hc + b)) = \\ -\frac{1}{c}(\mathbf{u}''\mathcal{H}\mathbf{u}')\mathbf{s} + \frac{1}{c}(\mathbf{s}'\mathcal{H}\mathbf{u}')\mathbf{u}' - \frac{g\mu c\mathbf{u}'}{\sqrt{c^2\|\mathbf{u}'\|^2 + (\mathbf{s} \cdot \mathbf{u}')^2}} \\ \cdot \left(1 + \frac{\mathbf{u}''\mathcal{H}\mathbf{u}'}{gc}\right)_+, \end{aligned} \quad (\text{A6})$$

where $\nabla_{\mathbf{x}}$ is the gradient vector in the horizontal x, y plane and g acceleration due to gravity. The subscript $+$ stands for the positive part, $x_+ = \max(0, x)$. The system (A5) and (A6), is obtained using a trick that consists of performing an asymptotic analysis of the free surface incompressible Navier-Stokes equations although the final model is not based on the Navier-Stokes equations; that is, viscous effects are not accounted for. Equations (A5) and (A6) are obtained by this asymptotic analysis up to errors $\mathcal{O}(\epsilon^3)$ and $\mathcal{O}(\epsilon^2)$ respectively for mass and velocity equations, as the aspect ratio ϵ approaches 0. It is obtained by assuming that the viscosity $\nu = \mathcal{O}(\epsilon^2)$, the Coulomb bottom friction coefficient $\mu = \mathcal{O}(\nu/\epsilon)$, and the curvature $\mathcal{H} = \mathcal{O}(\epsilon)$ [Bouchut and Westdickenberg, 2004]. The model is invariant with respect to rotation, admits a conservative energy equation and preserves the steady state of a lake at rest. For flow over an inclined plane, the case considered here, the equations can be reduced to (3) and (4).

Appendix B

[74] The numerical method in the one-dimensional case has been discussed by Mangeney-Castelnau *et al.* [2005], and we will review only the formulas here before extending the method to two dimensions.

B1. Saint Venant Problem With Topography and Friction in One Dimension

[75] Let us first describe the 1-D scheme in order to present the basic principles of the numerical method. The one-dimensional Saint Venant system with topography and friction is expressed as

$$\begin{cases} \partial_t h + \partial_x(hu) = 0, \\ \partial_t(hu) + \partial_x(hu^2 + gh^2/2) + hgb_x = hf, \end{cases} \quad (\text{B1})$$

where $b(x)$ represents topography and b_x the derivative of b as a function of x , and where the friction force $f = f(t, x)$ must satisfy

$$\begin{cases} |f(t, x)| \leq g\mu, \\ u(t, x) \neq 0 \Rightarrow f(t, x) = -g\mu \frac{u(t, x)}{|u(t, x)|}. \end{cases} \quad (\text{B2})$$

The 1-D version of the system (2)–(7) is of the form (A7)–(A8) after a slight change of notation (from (2)–(4) and (7), define $x' = x/c$, $g' = gc$, $b' = b/c$, and use these new variables in order to identify the system with (A7)–(A8)). In this system the steady states at rest play a crucial role and are given by $u = 0$, $f = \partial_x(gh + gb)$, or equivalently,

$$u = 0 \quad \text{and} \quad |\partial_x(h + b)| \leq \mu. \quad (\text{B3})$$

We are interested in using well-balanced schemes, i.e., schemes that preserve steady states at the discrete level. The apparent topography approach considers the source term as a topography by defining $g\partial_x b = -f$. Consider a 1-D mesh made of cells of size Δx . The cells are defined by

$$C_i =]x_{i-1/2}, x_{i+1/2}[\quad (\text{B4})$$

of length $\Delta x_i = x_{i+1/2} - x_{i-1/2}$. The cell centers are denoted $x_i = (x_{i+1/2} + x_{i-1/2})/2$. We consider a time step Δt and define the discrete times by $t_n = n\Delta t$, with $n \in \mathbb{N}$. According to *Mangeney-Castelnau et al.* [2005], this leads to the following formulas,

$$\mathbf{U}_i^{n+1} - \mathbf{U}_i^n + \frac{\Delta t}{\Delta x_i} (\mathbf{F}_{i+1/2-} - \mathbf{F}_{i-1/2+}) = 0, \quad (\text{B5})$$

where \mathbf{U}_i^n

$$\mathbf{U}_i^n \simeq \frac{1}{\Delta x_i} \int_{C_i} \mathbf{U}(t_n, x) dx \quad (\text{B6})$$

is an approximation of the average of the exact solution at time t_n

$$\mathbf{U} = \begin{pmatrix} h \\ hu \end{pmatrix} \quad (\text{B7})$$

over the cell C_i . The left/right numerical fluxes are computed as

$$\begin{aligned} \mathbf{F}_{i+1/2-} &= \mathbf{F}_l(\mathbf{U}_i, \mathbf{U}_{i+1}, \Delta b_{i+1/2} + \Delta \tilde{b}_{i+1/2}^n) \\ \mathbf{F}_{i+1/2+} &= \mathbf{F}_r(\mathbf{U}_i, \mathbf{U}_{i+1}, \Delta b_{i+1/2} + \Delta \tilde{b}_{i+1/2}^n), \end{aligned} \quad (\text{B8})$$

with $\Delta b_{i+1/2} = b_{i+1} - b_i$, and

$$g\Delta \tilde{b}_{i+1/2}^n = -f_{i+1/2}^n \Delta x. \quad (\text{B9})$$

[76] The numerical fluxes \mathbf{F}_l and \mathbf{F}_r are derived by the hydrostatic reconstruction method [Audusse et al., 2004], and have the following form:

$$\begin{aligned} \mathbf{F}_l(\mathbf{U}_l, \mathbf{U}_r, \Delta b) &= \mathcal{F}(\mathbf{U}_l^*, \mathbf{U}_r^*) + \begin{pmatrix} 0 \\ \frac{g}{2} h_l^2 - \frac{g}{2} h_r^2 \end{pmatrix} \\ \mathbf{F}_r(\mathbf{U}_l, \mathbf{U}_r, \Delta b) &= \mathcal{F}(\mathbf{U}_l^*, \mathbf{U}_r^*) + \begin{pmatrix} 0 \\ \frac{g}{2} h_r^2 - \frac{g}{2} h_l^2 \end{pmatrix}, \end{aligned} \quad (\text{B10})$$

where $\mathbf{U}_l^* = (h_{l*}, h_{l*}u_l)$, $\mathbf{U}_r^* = (h_{r*}, h_{r*}u_r)$, and

$$\begin{aligned} h_{l*} &= \max(0, h_l - \max(0, \Delta b)) \\ h_{r*} &= \max(0, h_r - \max(0, -\Delta b)). \end{aligned} \quad (\text{B11})$$

[77] Here \mathcal{F} is any entropy satisfying consistent numerical flux for the homogeneous problem (i.e., without topography and friction), that is capable of dealing with dry states. We use a relaxation solver described by *Bouchut* [2004], but other choices give similar results.

[78] Then, if $f_{i+1/2}^n$ is a consistent value for the friction, it is easy to see that our scheme is consistent with (A7) and well-balanced since it preserves the discrete steady states satisfying $u_i = u_{i+1} = 0$ and $gh_{i+1} - gh_i + g\Delta b_{i+1/2} = f_{i+1/2}^n \Delta x$. The scheme also conserves mass, is capable of computing dry bed states and satisfies a discrete entropy inequality. For the computation of $f_{i+1/2}^n$, a good choice is

$$f_{i+1/2}^n = -g \text{proj}_\mu \left(\frac{h_i - h_{i+1} - \Delta b_{i+1/2}}{\Delta x} + \frac{u_{i+1/2}}{g\Delta t} \right), \quad (\text{B12})$$

where

$$\text{proj}_\mu(X) = \begin{cases} X & \text{if } |X| \leq \mu, \\ \mu \frac{X}{|X|} & \text{if } |X| > \mu. \end{cases} \quad (\text{B13})$$

and, for example,

$$u_{i+1/2} = \frac{h_i u_i + h_{i+1} u_{i+1}}{h_i + h_{i+1}}. \quad (\text{B14})$$

This gives a well-balanced scheme, in the sense that data satisfying

$$u_i = 0 \quad \text{and} \quad |h_i - h_{i+1} - \Delta b_{i+1/2}| \leq \mu \Delta x \quad (\text{B15})$$

are preserved exactly. For higher precision, a better choice is to replace (B12) by

$$f_{i+1/2}^n = -g \text{Proj}_\mu \left(\frac{h_i - h_{i+1} - \Delta b_{i+1/2}}{\Delta x}, \frac{u_{i+1/2}}{g\Delta t} \right), \quad (\text{B16})$$

where

$$\text{Proj}_\mu(X, Y) = \text{proj}_\mu \left(\text{proj}_\mu(X) + \frac{2}{1 + \max(1, -X \cdot Y/\mu|Y|)} Y \right). \quad (\text{B17})$$

For models where $\mu = \mu(h, u)$, the definitions can easily be extended using local values $\mu_{i+1/2}$ in (B12) or (B17). The numerical processing of the friction presented above leads to a regularization of the friction for small velocities. Actually, in the case of small velocity, equations (B12) or (B17) compute a friction force directed opposite to the sum of h and b gradients (i.e., the gradient of pressure added to the force of gravity) and set its norm equal to the norm of this sum.

B2. Two-Dimensional Scheme

[79] The two-dimensional Saint Venant system with topography and friction is written

$$\begin{cases} \partial_t h + \partial_x(hu) + \partial_y(hv) = 0 \\ \partial_t(hu) + \partial_x(hu^2 + gh^2/2) + \partial_y(huv) + hg\partial_x b = hf_x \\ \partial_t(hv) + \partial_x(huv) + \partial_y(hv^2 + gh^2/2) + hg\partial_y b = hf_y, \end{cases} \quad (\text{B18})$$

where $b(x, y)$ represents the 2-D topography and where the friction force $\mathbf{f}(t, x, y) = (f_x, f_y)$ must satisfy

$$\begin{cases} \|\mathbf{f}(t, x, y)\| \leq g\mu \\ \mathbf{u}(t, x, y) \neq \mathbf{0} \Rightarrow \mathbf{f}(t, x, y) = -g\mu \frac{\mathbf{u}(t, x, y)}{\|\mathbf{u}(t, x, y)\|}, \end{cases} \quad (\text{B19})$$

with $\mathbf{u} = (u, v)$. As explained in section 9.1 The system (2)–(4) and (7) is of the form (B18)–(B19) after a slight change of notation. As in the 1-D case, we will describe the scheme for (B18)–(B19). In this system the steady states at rest are given by $\mathbf{u} = 0$, $\mathbf{f} = \nabla_x(gh + gb)$, or, equivalently,

$$\mathbf{u} = 0 \quad \text{and} \quad \|\nabla_x(h + b)\| \leq \mu. \quad (\text{B20})$$

[80] As usual, the 2-D finite volume method is performed using the 1-D scheme interface by interface. Note that the 1-D system corresponding to (B18) is (A7) with the addition of the advection equation $\partial_t(hv) + \partial_x(huv) = 0$.

[81] Consider a two-dimensional mesh made of rectangles of sizes $\Delta x, \Delta y$. The rectangles shall be defined by subscripts (i, j) , and the interfaces between two adjacent rectangles by $(i + 1/2, j)$ and $(i, j + 1/2)$. The approximate value of

$$\mathbf{U} = \begin{pmatrix} h \\ hu \\ hv \end{pmatrix} \quad (\text{B21})$$

over the rectangle (i, j) is denoted by \mathbf{U}_{ij}^n , where n refers to the time level (not always indicated here for simplicity). The solution \mathbf{U} and the numerical fluxes \mathbf{F} are 3-D vectors but will be written here in bold symbols for the sake of simplicity. Then, the two-dimensional scheme is written

$$\begin{aligned} \mathbf{U}_{ij}^{n+1} - \mathbf{U}_{ij}^n + \frac{\Delta t}{\Delta x} (\mathbf{F}_{i+1/2-j} - \mathbf{F}_{i-1/2+j}) \\ + \frac{\Delta t}{\Delta y} (\mathbf{F}_{i,j+1/2-} - \mathbf{F}_{i,j-1/2+}) = 0, \end{aligned} \quad (\text{B22})$$

where the interface fluxes are computed via

$$\begin{aligned} \mathbf{F}_{i+1/2+j} &= \mathbf{F}_{l/r}(\mathbf{U}_{ij}, \mathbf{U}_{i+1,j}, \Delta b_{i+1/2,j} + \Delta \tilde{b}_{i+1/2,j}) \\ \mathbf{F}_{i,j+1/2+} &= \hat{\mathbf{F}}_{l/r}(\hat{\mathbf{U}}_{ij}, \hat{\mathbf{U}}_{i,j+1}, \Delta b_{i,j+1/2} + \Delta \tilde{b}_{i,j+1/2}). \end{aligned} \quad (\text{B23})$$

[82] In (B23), we denote $\Delta b_{i+1/2,j} = b_{i+1,j} - b_{ij}$, $\Delta b_{i,j+1/2} = b_{i,j+1} - b_{ij}$, $\hat{\mathbf{U}} = (h, hv, hu)$ if $\mathbf{U} = (h, hu, hv)$. The 2-D numerical fluxes are defined as follows if $\mathbf{U}_l = (h_l, h_l u_l, h_l v_l)$ and $\mathbf{U}_r = (h_r, h_r u_r, h_r v_r)$,

$$\begin{aligned} \mathbf{F}_{l/r}(\mathbf{U}_l, \mathbf{U}_r, \Delta b) &= (\mathbf{F}_{l/r}(h_l, h_l u_l, h_r, h_r u_r, \Delta b) \\ &\quad \cdot F_{l/r}^h(h_l, h_l u_l, h_r, h_r u_r, \Delta b) v_*, \end{aligned} \quad (\text{B24})$$

where $F_{l/r}$ are the one-dimensional fluxes (B10)–(B11), the power h refers to the first component (note that $F_l^h = F_r^h$), and

$$v_* = \begin{cases} v_l & \text{if } F_{l/r}^h(h_l, h_l u_l, h_r, h_r u_r, \Delta b) \geq 0 \\ v_r & \text{if } F_{l/r}^h(h_l, h_l u_l, h_r, h_r u_r, \Delta b) \leq 0. \end{cases} \quad (\text{B25})$$

The apparent topography terms are related to the friction forces by

$$\begin{aligned} g\Delta \tilde{b}_{i+1/2,j} &= -(f_{i+1/2,j})_x \Delta x \\ g\Delta \tilde{b}_{i,j+1/2} &= -(f_{i,j+1/2})_y \Delta y, \end{aligned} \quad (\text{B26})$$

where the indices x and y relate to the x and y components respectively. According to the multidimensional finite volume formulation of well-balanced schemes of Bouchut [2004], note that the x fluxes in (B22) involve the x component of \mathbf{f} , while the y fluxes involve the y component of \mathbf{f} . Finally, the friction terms are computed by the projections

$$\begin{aligned} \mathbf{f}_{i+1/2,j} &= -g \text{Proj}_\mu \left(\left(\frac{h_{ij} - h_{i+1,j} - \Delta b_{i+1/2,j}}{\Delta x}, 0 \right) \cdot \frac{\mathbf{u}_{i+1/2,j}}{g\Delta t} \right) \\ \mathbf{f}_{i,j+1/2} &= -g \text{Proj}_\mu \left(\left(0, \frac{h_{ij} - h_{i,j+1} - \Delta b_{i,j+1/2}}{\Delta y} \right) \cdot \frac{\mathbf{u}_{i,j+1/2}}{g\Delta t} \right), \end{aligned} \quad (\text{B27})$$

where Proj is still defined by (B23) but with \mathbf{X}, \mathbf{Y} two-dimensional vectors, and

$$\begin{aligned} \mathbf{u}_{i+1/2,j} &= \frac{h_{ij}\mathbf{u}_{ij} + h_{i+1,j}\mathbf{u}_{i+1,j}}{h_{ij} + h_{i+1,j}} \\ \mathbf{u}_{i,j+1/2} &= \frac{h_{ij}\mathbf{u}_{ij} + h_{i,j+1}\mathbf{u}_{i,j+1}}{h_{ij} + h_{i,j+1}}. \end{aligned} \quad (\text{B28})$$

[83] **Acknowledgments.** We thank R. Iverson and K. Hutter for their insight and comments that have greatly improved this paper. We thank B. Perthame for fruitful discussions. We thank the members of the GdR MiDi for interesting remarks. This work was supported by the Action Concertée Incitative Nouvelles Interfaces des Mathématiques (CNRS), the Action Concertée Incitative Jeunes Chercheurs (CNRS), and the ACI Aléas et Changements Globaux (CNRS). This is contribution IPGP 2176.

References

- Audusse, E., F. Bouchut, M. O. Bristeau, R. Klein, and B. Perthame (2004), A fast and stable well-balanced scheme with hydrostatic reconstruction for shallow water flows, *SIAM J. Sci. Comput.*, 25, 2050–2065.
- Bouchut, F. (2004), *Nonlinear Stability of Finite Volume Methods for Hyperbolic Conservation Laws, and Well-Balanced Schemes for Sources*, *Frontiers Math. Ser.*, Springer, New York.
- Bouchut, F., and M. Westdickenberg (2004), Gravity driven shallow water models for arbitrary topography *Commun. Math. Sci.*, 2, 359–389.
- Calder, E. S., R. S. J. Sparks, and M. C. Gardeweg (2000), Erosion, transport and segregation of pumice and lithic clasts in pyroclastic flows inferred from ignimbrite at Lascar Volcano, Chile, *J. Volcanol. Geotherm. Res.*, 104, 201–235.
- Da Cruz, F. (2004), *Ecoulement de grains secs: Frottement et blocage*, Ph.D. thesis, Ecole Natl. des Ponts et Chaussées, Marne la Vallée, France.
- Dade, W. B., and H. E. Huppert (1998), Long runout rockfalls, *Geology*, 26, 803–806.
- Daerr, A., and S. Douady (1999), Two types of avalanche behaviour in granular media, *Nature*, 399, 241–243.
- Deboeuf, S. (2005), *Transition et coexistence solide-liquide dans les matériaux granulaires*, Ph.D. thesis, Inst. de Phys. du Globe de Paris, Paris, France.

- Deboeuf, S., O. Dauchot, L. Staron, A. Mangeney, and J. P. Vilotte (2005a), Memory of the unjamming transition during cyclic tiltings of a granular pile, *Phys. Rev. E*, **72**, 051305.
- Deboeuf, S., O. Dauchot, L. Staron, J. P. Vilotte, and A. Mangeney (2005b), Evolution of the contact network during tilting cycles of a granular pile under gravity, in *Powders and Grains*, edited by R. Garcia-Rojo, H. J. Herrmann, and S. McNamara, pp. 105–108, A. A., Balkema, Brookfield, Vt.
- Deboeuf, S., E. Lajeunesse, O. Dauchot, and B. Andreotti (2006), Flow rule, self-channelization and levees in unconfined granular flows *Phys. Rev. E*, **73**, 158303.
- Denlinger, R. P., and R. M. Iverson (2001), Flow of variably fluidized granular masses across three-dimensional terrain: 2. Numerical predictions and experimental tests, *J. Geophys. Res.*, **106**, 553–566.
- Denlinger, R. P., and R. M. Iverson (2004), Granular avalanches across irregular three-dimensional terrain: 1. Theory and computation, *J. Geophys. Res.*, **109**, F01014, doi:10.1029/2003JF000085.
- Douady, S., B. Andreotti, and A. Daerr (1999), On granular surface flow equations, *Eur. Phys. J. B*, **11**, 131–142.
- Ertas, D., G. S. Grest, T. C. Halsey, D. Levine, and L. Silbert (2001), Gravity-driven dense granular flows, *Europhys. Lett.*, **56**, 214–220.
- Félix, G., and N. Thomas (2004), Relation between dry granular flow regimes and morphology of the deposits: Formation of levées in pyroclastic deposits, *Earth Planet. Sci. Lett.*, **221**, 197–231.
- Forterre, Y., and O. Pouliquen (2003), Long-surface-wave instability in dense granular flows, *J. Fluid Mech.*, **486**, 21–50.
- Gray, J. M. N. T., M. Wieland, and K. Hutter (1999), Gravity driven free surface flow of granular avalanches over complex basal topography, *Proc. R. Soc. London, Ser. A*, **455**, 1841–1874.
- Hutter, K., and T. Koch (1991), Motion of a granular avalanche in an exponentially curved chute: Experiments and theoretical predictions, *Philos. Trans. R. Soc. London, Ser. A*, **334**, 93–138.
- Hutter, K., T. Koch, C. Pluss, and S. B. Savage (1995), The dynamics of avalanches of granular materials from initiation to run out. part II, Experiments, *Acta Mech.*, **109**, 127–165.
- Iverson, R. M., and R. P. Denlinger (2001), Flow of variably fluidized granular masses across three-dimensional terrain: 1. Coulomb mixture theory, *J. Geophys. Res.*, **106**, 537–552.
- Iverson, R. M., and J. Vallance (2001), New views of granular mass flows, *Geology*, **29**, 115–118.
- Iverson, R. M., M. Logan, and R. P. Denlinger (2004), Granular avalanches across irregular three-dimensional terrain: 2. Experimental tests, *J. Geophys. Res.*, **109**, F01015, doi:10.1029/2003JF000084.
- Jop, P., Y. Forterre, and O. Pouliquen (2005), Crucial role of sidewalls in granular surface flows: Consequences for the rheology, *J. Fluid Mech.*, **541**, 167–192.
- Kelfoun, K., and T. H. Druitt (2005), Numerical modeling of the emplacement of Socompa rock avalanche, Chile, *J. Geophys. Res.*, **110**, B12202, doi:10.1029/2005JB003758.
- Klaucke, I., D. G. Masson, N. H. Kenyon, and J. V. Gardner (2004), Sedimentary processes on the lower Monterey Fan Channel and channel-mouth lobe, *Mar. Geol.*, **206**, 181–198.
- Lucas, A., and A. Mangeney (2007), Mobility and topographic effects for large Valles Marineris landslides on Mars, *Geophys. Res. Lett.*, doi:10.1029/2007GL029835, in press.
- Malin, M. C., and K. S. Edgett (2000), Evidence for recent groundwater seepage and surface runoff on Mars, *Science*, **228**, 2330–2335.
- Mangeney-Castelnau, A., J.-P. Vilotte, M. O. Bristeau, B. Perthame, F. Bouchut, C. Simeoni, and S. Yerneni (2003), Numerical modeling of avalanches based on Saint Venant equations using a kinetic scheme, *J. Geophys. Res.*, **108**(B11), 2527, doi:10.1029/2002JB002024.
- Mangeney-Castelnau, A., F. Bouchut, J. P. Vilotte, E. Lajeunesse, A. Aubertin, and M. Pirulli (2005), On the use of Saint Venant equations to simulate the spreading of a granular mass, *J. Geophys. Res.*, **110**, B09103, doi:10.1029/2004JB003161.
- Mangold, N., F. Costard, and F. Forget (2003), Debris flows over sand dunes on Mars: Evidence for liquid water, *J. Geophys. Res.*, **108**(E4), 5027, doi:10.1029/2002JE001958.
- McDonald, R. R., and R. S. Anderson (1996), Constraints on eolian grain flow dynamics through laboratory experiments on sand slope, *J. Sediment. Res.*, **66**, 642–653.
- McDougall, S., and O. Hungr (2004), A model for the analysis of rapid landslide runout motion across three-dimensional terrain, *Can. Geotech. J.*, **41**, 1084–1097.
- Naaim, M., S. Vial, and R. Couture (1997), Saint Venant approach for rock avalanches modelling, paper presented at the Saint Venant Symposium, Paris, 28–29 Aug.
- Naim, I. A., and S. Self (1978), Explosive eruptions and pyroclastic avalanches from Ngauruhoe in February 1975, *J. Volcanol. Geotherm. Res.*, **3**, 39–60.
- Pastor, M., J. A. Fernández Merodo, M. Quecedo, M. I. Herreros, E. González, and P. Mira (2002), Modelling of debris flows and flow slides, *Numer. Modell. Geomech.*, **6**, 1213–1232.
- Pirulli, M., A. Mangeney, M. O. Bristeau, and C. Scavia (2007), The effect of the Earth pressure coefficients on the runout of granular materials, *Environm. Modell. Software*, in press.
- Pitman, E. B., C. C. Nichita, A. K. Patra, A. C. Bauer, M. Sheridan, and M. Bursik (2003), Computing granular avalanches and landslides, *Phys. Fluids*, **15**, 3638–3646.
- Pouliquen, O. (1999), Scaling laws in granular flows down rough inclined planes, *Phys. Fluids*, **11**, 542–548.
- Pouliquen, O., and Y. Forterre (2002), Friction law for dense granular flows: Application to the motion of a mass down a rough inclined plane, *J. Fluid Mech.*, **453**, 133–151.
- Quarení, F., A. Tallarico, and M. Dragoni (2004), Modeling of the steady-state temperature field in lava flow levés, *J. Volcanol. Geotherm. Res.*, **132**, 241–251.
- Roberts, A. W. (1965), An investigation of the gravity flow of noncohesive materials through discharge chutes, *Trans. ASME*, **91**, 373–381.
- Rodriguez-Elizarraras, S., C. Siebe, J. C. Komorowski, J. M. Expindola, and R. Saucedo (1991), Field observations of pristine block and ash flow deposits emplaced April 16–17, 1991 at Volcan de Colimá, México, *J. Volcanol. Geotherm. Res.*, **48**, 399–412.
- Rowley, P. D., M. A. Kuntz, and N. S. MacLeod (1991), Pyroclastic-flow deposits, *U.S. Geol. Surv. Prof. Pap.*, **1250**, 489–512.
- Sakimoto, S. E. H., and T. K. P. Gregg (2001), Channeled flow: Analytic solutions, laboratory experiments, and applications to lava flows, *J. Geophys. Res.*, **106**, 8629–8644.
- Saucedo, R., J. L. Macas, M. I. Bursik, J. C. Mora, J. C. Gavilanes, and A. Cortes (2002), Emplacement of pyroclastic flows during the 1998–1999 eruption of Volcan de Colima, México, *J. Volcanol. Geotherm. Res.*, **117**, 129–153.
- Savage, S. B. (1979), Gravity flow of cohesionless granular materials in chutes and channels, *J. Fluid Mech.*, **92**, 53–96.
- Savage, S. B., and K. Hutter (1989), The motion of a finite mass of granular material down a rough incline, *J. Fluid Mech.*, **199**, 177–215.
- Sheridan, M. F., A. J. Stinton, A. Patra, E. B. Pitman, A. Bauer, and X. Nichita (2007), Evaluating TITAN2D mass-flow model using the 1963 Little Tahoma Peak avalanches, Mount Rainier, Washington, *J. Volcanol. Geotherm. Res.*, in press.
- Sokolovski, V. (1965), *Statics of Granular Media*, Elsevier, New York.
- Taberlet, N., P. Richard, A. Vallance, W. Losert, J. M. Pasini, J. T. Jenkins, and R. Delannay (2003), Superstable granular heap in a thin channel, *Phys. Rev. Lett.*, **91**, 264301.
- Tai, Y. C., S. Noelle, N. Gray, and K. Hutter (2002), Shock capturing and front tracking methods for granular avalanches, *J. Comput. Phys.*, **175**, 269–301.
- Treiman, A. H., and M. Y. Louge (2004), Martian slope streaks and Gullies: Origins as dry granular flows, *Lunar Planet. Sci.*, (XXXV), abstract 1323.
- Ui, T., N. Matsuwo, M. Sumita, and A. Fujinawa (1999), Generation of block and ash flows during the 1990–1995 eruption of Unzen volcano, Japan, *J. Volcanol. Geotherm. Res.*, **89**, 123–137.
- Wilson, L., and J. W. Head (1981), Morphology and rheology of pyroclastic flows and their deposits, and guidelines for future observations, *U.S. Geol. Surv. Bull.*, **1250**, 513–524.
- Yamamoto, T., S. Takarada, and S. Suto (1993), Pyroclastic flows from the 1991 eruption of Unzen volcano, *Japan, Bull. Volcanol.*, **55**, 166–175.

F. Bouchut, Département de Mathématique et Applications, Ecole Normale Supérieure, 45 rue d'Ulm, F-75230 Paris cedex 05, France. (fbouchut@dma.ens.fr)

M. O. Bristeau, INRIA, Projet BANG, BP105, F-78153 Le Chesnay cedex, France. (marie.odile.bristeau@inria.fr)

A. Mangeney, Institute for Nonlinear Science, University of California, San Diego, CMRR Building, 9500 Gilman Drive, La Jolla, CA 92093-0402, USA. (amangeney@ucsd.edu)

N. Thomas, IUSTI, CNRS, 5 rue E. Fermi, Technopole de Chateau-Gombert, F-13453 Marseille, France. (nathalie.thomas@polytech.univ-mrs.fr)

J. P. Vilotte, Equipe de Sismologie, Institut de Physique du Globe de Paris, 4 place Jussieu, F-75252 Paris cedex 05, France. (vilotte@ipgp.jussieu.fr)